



ATLAS NOTE

ATLAS-CONF-2016-077

4th August 2016



Search for a Scalar Partner of the Top Quark in the Jets+ E_T^{miss} Final State at $\sqrt{s} = 13$ TeV with the ATLAS detector

The ATLAS Collaboration

Abstract

A search for direct pair production of a scalar partner to the top quark in events with four or more jets plus missing transverse momentum is presented. An analysis of 13.3 fb^{-1} of $\sqrt{s} = 13$ TeV proton-proton collisions collected using the ATLAS detector at the LHC yielded no significant excess over the Standard Model background expectation. In the supersymmetric interpretation, the top squark is assumed to decay via $\tilde{t} \rightarrow t \tilde{\chi}_1^0$, $\tilde{t} \rightarrow b \tilde{\chi}_1^\pm \rightarrow b W^{(*)} \tilde{\chi}_1^0$, or $\tilde{t} \rightarrow b W \tilde{\chi}_1^0$, where $\tilde{\chi}_1^0$ ($\tilde{\chi}_1^\pm$) denotes the lightest neutralino (chargino). Exclusion limits are reported in terms of the top squark and neutralino masses. Assuming branching fractions of 100% to $t \tilde{\chi}_1^0$, top squark masses in the range 310–820 GeV are excluded for $\tilde{\chi}_1^0$ masses below 160 GeV. In the case where $m_{\tilde{t}} \sim m_t + m_{\tilde{\chi}^0}$ top squark masses between 23–380 GeV are excluded. Limits are also reported in terms of simplified models describing the associated production of dark matter (χ) with top quark pairs through a (pseudo)scalar mediator; models with a global coupling of 3.5, mediator masses up to 300 GeV, and χ masses below 40 GeV are excluded.

1. Introduction

Supersymmetry (SUSY) is an extension of the Standard Model (SM) that can resolve the gauge hierarchy problem [1–6] by introducing supersymmetric partners of the known bosons and fermions. The SUSY partner to the top quark, the top squark¹ (\tilde{t}), plays an important role in canceling the dominant top quark loop diagram contributions to the divergence of the Higgs boson mass.

In R -parity conserving SUSY models [7–10], the supersymmetric partners are produced in pairs. The cross section for direct pair production of top squarks is given by gluon-gluon and $q\bar{q}$ fusion and is largely decoupled from SUSY model parameters [11–13]. The decay of the top squark depends on the masses, the mixing of the left- and right-handed \tilde{t} quarks and the mixing parameters of the fermionic partners of the electroweak and Higgs bosons which are collectively known as charginos, $\tilde{\chi}_i^\pm$, $i = 1, 2$ and neutralinos, $\tilde{\chi}_i^0$, $i = 1–4$. Three different decay modes are considered: (a) $\tilde{t} \rightarrow t\tilde{\chi}_1^0$, (b) $\tilde{t} \rightarrow b\tilde{\chi}_1^\pm \rightarrow bW^{(*)}\tilde{\chi}_1^0$, or (c) $\tilde{t} \rightarrow bW\tilde{\chi}_1^0$, as illustrated in Fig. 1(a)–(c), respectively. The lightest neutralino, $\tilde{\chi}_1^0$, is assumed to be the stable, weakly interacting lightest supersymmetric particle² that also serves as a dark matter candidate [14, 15].

In addition to direct pair production, top squarks can be produced indirectly through gluino decays, as shown in Fig. 1(d). This search considers models where the mass difference between the top squark and the neutralino is small, i.e., $\Delta m(\tilde{t}, \tilde{\chi}_1^0) = 5$ GeV. In this scenario, the jets originating from the \tilde{t} decays have small momenta compared to experimental acceptance resulting in a nearly identical signature to $\tilde{t} \rightarrow t\tilde{\chi}_1^0$ signal models.

Finally, a simplified model of top quark pairs produced in association with a pair of dark matter (DM) particles is also considered [16, 17]. As illustrated in Fig. 1(e), a pair of DM particles (each represented by χ) are produced via a spin-0 mediator (φ or a). This mediator can be a scalar or pseudoscalar and is coupled to the SM particles by mixing with the SM Higgs or extended Higgs sector.

This note presents the search for direct top squark pair production using $\int \mathcal{L} dt = (13.3 \pm 0.4) \text{ fb}^{-1}$ of pp collisions provided by the Large Hadron Collider (LHC) at a center-of-mass energy of $\sqrt{s} = 13$ TeV. These data were collected by the ATLAS detector in 2015 and 2016. All-hadronic final states with at least four jets and large missing transverse momentum ($\mathbf{p}_T^{\text{miss}}$, whose magnitude is referred to as E_T^{miss}) are considered, and the results are interpreted according to a variety of signal models as described above. Signal regions are defined to maximize the experimental sensitivity over a large range of kinematic phase space with various specializations. Sensitivity to high top squark masses ~ 850 GeV (as in Fig. 1(a)) and top squarks produced through gluino decays (as in Fig. 1(d)) are achieved by exploiting techniques designed to reconstruct Lorentz-boosted top quarks. The dominant SM background process for this kinematic region is $Z \rightarrow \nu\bar{\nu}$ plus heavy flavor jets. The sensitivity to the decay $b\tilde{\chi}_1^\pm$ is enhanced by vetoing events containing hadronically decaying top quark candidates. Sensitivity to the region where $m_{\tilde{t}} - m_{\tilde{\chi}_1^0} \sim m_t$, which nominally has low- p_T final state objects and low E_T^{miss} , is achieved by exploiting events in which initial state radiation (ISR) boosts the di-top-squark system in the transverse plane. For this regime, $t\bar{t}$ production makes up the dominant background contribution. Similar searches based on $\sqrt{s} = 7$ TeV and $\sqrt{s} = 8$ TeV data collected at Run 1 of the LHC have been performed by both the ATLAS [18, 19] and CMS [20–25] collaborations.

¹ The superpartners of the left- and right-handed top quarks, \tilde{t}_L and \tilde{t}_R , mix to form the two mass eigenstates \tilde{t}_1 and \tilde{t}_2 , where \tilde{t}_1 is the lighter one. Throughout this note \tilde{t}_1 is noted as \tilde{t} .

² However, the lightest supersymmetric particle could also be a very light gravitino (the fermionic partner of the graviton), which would evade existing model-dependent limits on the neutralino mass.

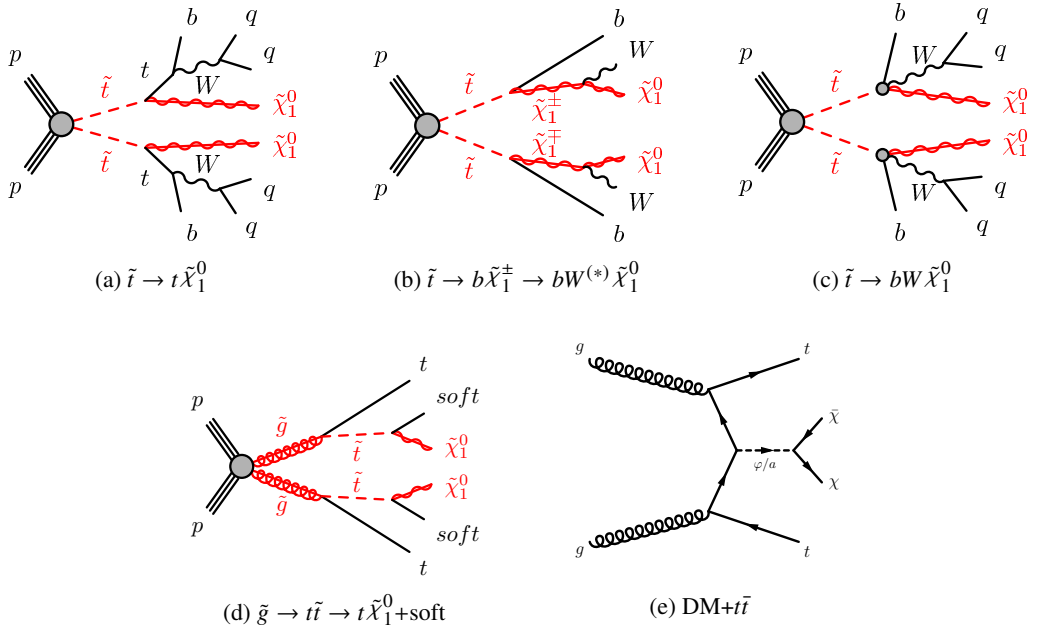


Figure 1: The decay topologies of the signal models considered with experimental signatures of four or more jets plus missing transverse momentum.

The following sections detail the ATLAS detector, trigger and data collection, as well as the simulated event samples used in the analysis. This is followed by a description of the event and physics object reconstruction and the signal region definitions. The procedures and control regions used to estimate the backgrounds in each of the signal regions are described, as well as the evaluation of systematic uncertainties, followed by the presentation of the results and their interpretation.

2. ATLAS detector

The ATLAS experiment [26] at the LHC is a multi-purpose particle detector with a forward-backward symmetric geometry³ and a near 4π coverage in solid angle. It consists of an inner tracking detector surrounded by a thin superconducting solenoid providing a 2 T axial magnetic field, electromagnetic and hadron calorimeters, and a muon spectrometer. The inner tracking detector covers the pseudorapidity range $|\eta| < 2.5$. It consists of silicon pixel, silicon micro-strip, and transition radiation tracking detectors. The newly installed innermost layer of pixel sensors [27] was operational for the first time during the 2015 data taking. Lead/liquid-argon (LAr) sampling calorimeters provide electromagnetic (EM) energy measurements with high granularity. A hadron (steel/scintillator-tile) calorimeter covers the central pseudorapidity range ($|\eta| < 1.7$). The end-cap and forward regions are instrumented with LAr calorimeters

³ ATLAS uses a right-handed coordinate system with its origin at the nominal interaction point (IP) in the centre of the detector and the z -axis along the beam pipe. The x -axis points from the IP to the centre of the LHC ring, and the y -axis points upwards. Cylindrical coordinates (r, ϕ) are used in the transverse plane, ϕ being the azimuthal angle around the z -axis. The pseudorapidity is defined in terms of the polar angle θ as $\eta = -\ln \tan(\theta/2)$. Angular distance is measured in units of $\Delta R \equiv \sqrt{(\Delta\eta)^2 + (\Delta\phi)^2}$.

for both EM and hadronic energy measurements up to $|\eta| = 4.9$. The muon spectrometer surrounds the calorimeters and is based on three large air-core toroid superconducting magnets with eight coils each. The toroid field strength is 0.5 T in the central region and 1 T in the end-cap regions. It includes a system of precision tracking chambers and fast detectors for triggering.

3. Trigger and data collection

The data were collected from August to November 2015 and April to July 2016 at a pp centre-of-mass energy of 13 TeV with 25 ns bunch spacing. A two-level trigger system is used to select events. The first-level trigger is implemented in hardware and uses a subset of the detector information to reduce the accepted rate to at most 100 kHz. This is followed by a software-based trigger that reduces the accepted event rate to 1 kHz for offline storage.

For the primary search region, a missing transverse momentum trigger was used for 2015 data which bases the bulk of its rejection on the vector sum of transverse energies deposited in projective trigger towers (each with a size of approximately $\Delta\eta \times \Delta\phi \sim 0.1 \times 0.1$ for $|\eta| < 2.5$; these are larger and less regular in the more forward regions). A more refined calculation, based on the vector sum of all calorimeter cells, is used at a later stage in the trigger processing, requiring an energy threshold of 70 GeV. Due to the increase in instantaneous luminosity in 2016 data a higher threshold of 100 GeV is used with a different trigger algorithm which is based on the transverse vector sum of all reconstructed jets. Data events were collected using these triggers, which are fully efficient for offline calibrated $E_T^{\text{miss}} > 250$ GeV in signal events. The luminosity uncertainty of 2.1% (3.7%) for data taken in 2015 (2016) is derived following the same methodology as that detailed in Refs. [28] and [29], from a preliminary calibration of the luminosity scale obtained from beam-separation scans performed in August 2015 (May 2016).

Data samples enriched in the major sources of background were collected with electron or muon triggers. The electron trigger selects events based on the presence of clusters of energy in the electromagnetic calorimeter, with a shower shape consistent with that of an electron, and a matching track in the tracking system. The muon trigger selects events containing one or more muon candidates based on tracks identified in the muon spectrometer and inner detector. The transverse momentum threshold required by triggers in 2015 is 24 GeV for electrons and 20 GeV for muons. Due to the higher instantaneous luminosity in 2016 the trigger threshold was increased to 26 GeV for both electrons and muons and a tight isolation requirement is applied. In order to recover some of the efficiency for high- p_T leptons, events were also collected with single-electron and single-muon triggers with looser or no isolation requirements, but with higher p_T thresholds ($p_T > 60$ GeV and $p_T > 50$ GeV, respectively). Finally, a single-electron trigger requiring $p_T > 120$ GeV (in 2015) and $p_T > 140$ GeV (in 2016) with less restrictive electron identification criteria is used to increase the selection efficiency for high- p_T electrons. The electron and muon triggers used are $> 99\%$ efficient for electrons and muons with p_T of 2 GeV greater than the trigger thresholds.

Triggers based on the presence of high- p_T jets are used to collect data samples for the estimation of the multijet and all-hadronic $t\bar{t}$ background. The jet p_T thresholds ranged from 20 to 400 GeV. In order to stay within the bandwidth limits of the trigger system, only a fraction of events passing these triggers were recorded to permanent storage.

4. Simulated samples and signal modelling

Simulated events are used to model the SUSY signal and to aid in the description of the background processes. Several configurations are used for the signal samples, as shown in Fig. 1: (a) both top squarks decay via $\tilde{t} \rightarrow t \tilde{\chi}_1^0$, with $\Delta m(\tilde{t}, \tilde{\chi}_1^0) > m_t$, where m_t is the mass of the top quark, (b) both top squarks decay via $\tilde{t} \rightarrow b \tilde{\chi}_1^\pm \rightarrow b W^{(*)} \tilde{\chi}_1^0$, where $m(\tilde{\chi}_1^\pm) = 2m(\tilde{\chi}_1^0)$ which is motivated by gaugino universality, and (c) three body decays via $\tilde{t} \rightarrow b W \tilde{\chi}_1^0$, where $m(b) + m(W) < \Delta m(\tilde{t}, \tilde{\chi}_1^0) < m_t$. These signal samples are generated in a grid across the plane of the top squark and $\tilde{\chi}_1^0$ masses with a grid spacing of 50 GeV across most of the plane. Gluino-mediated \tilde{t} production is also simulated (as shown in Fig. 1(d)), in which gluinos decay via $\tilde{g} \rightarrow t \tilde{t}$, with the \tilde{t} always decaying to low momenta objects and $\tilde{\chi}_1^0$. The mass difference $\Delta m(\tilde{t}, \tilde{\chi}_1^0)$ is set to 5 GeV, and a range of gluino and top squark masses are generated.

Finally (as shown in Fig. 1(e)), the associated production of a $t\bar{t}$ pair and a pair of dark matter particles is simulated for a range of mediator and dark matter particle masses. In order to fulfill precision constraints from flavor measurements, the model assumes Yukawa-like couplings between the dark sector mediator and the SM fermions. This motivates the choice of studying these models in heavy flavor quark final states. The model has five free parameters [30, 31] corresponding to the mass of the mediator and the DM particle, the coupling of the mediator with the DM and SM particles, and the width of the mediator. The mediator width is assumed to be the minimal width that can be calculated from all parameters of the model. The signal grid is generated by scanning over the mass parameters. The coupling of the mediator to the dark matter particle (g_χ) is set to be equal to its coupling to the quarks (g_q) and cross sections corresponding to a range of couplings are considered. The minimum mediator coupling considered is 0.1 and the maximum mediator coupling considered is 3.5, at the perturbative limit, and has the same strength for SM and DM particles.

The aforementioned signal models are all generated with **MADGRAPH5_AMC@NLO** [32] interfaced to **PYTHIA 8** [33] for the parton showering (PS) and hadronisation and with **EvtGEN v1.2.0** program [34] as afterburner. The matrix element (ME) calculation is performed at tree-level and includes the emission of up to two additional partons for the \tilde{t} samples but not for the DM ones. The parton distribution function (PDF) set used for the generation of the \tilde{t} samples is **NNPDF2.3LO** [35] (**NNPDF3.0NLO** for the DM) and the A14 set [36] of underlying-event tuned parameters (UE tune). For the direct \tilde{t} pair production samples, the ME-PS matching is performed with the **CKKW-L** [37] prescription, with a matching scale set to one quarter of the mass of the \tilde{t} . Signal cross sections are calculated to next-to-leading order in the strong coupling constant, adding the resummation of soft gluon emission at next-to-leading-logarithmic accuracy (NLO+NLL) [11–13]. The nominal cross section and the uncertainty are taken from an envelope of cross section predictions using different PDF sets and factorization and renormalization scales, as described in Ref. [38].

SM background samples are generated with different MC generators depending on the process. The background sources of $Z + \text{jets}$ and $W + \text{jets}$ are generated with **SHERPAv2.2.0** [39] using **NNPDF3.0NNLO** [35] PDF set and the default tune. Top quark pair production where at least one of the top quarks decays to a lepton and single top production are simulated with **POWHEG-Boxv.2** [40] and interfaced to **PYTHIA6** [41] for PS and hadronisation, with **CT10** [42] PDF set and using the **P2012** [43] set of tuned parameters. **MADGRAPH5_AMC@NLO** interfaced to **PYTHIA 8** for PS and hadronisation is used to generate the $t\bar{t}+V$ samples at NLO with the **NNPDF3.0NLO** PDF set. The underlying tune used is A14 with the **NNPDF2.3LO** PDF set. Finally, dibosons are generated with **SHERPAv2.1.1** using **CT10** PDF set. Additional information can be found in Refs. [44–48].

The detector simulation [49] is performed using either GEANT4 [50] or a fast simulation framework where the showers in the electromagnetic and hadronic calorimeters are simulated with a parameterized description [51] and the rest of the detector is simulated with GEANT4. The fast simulation was validated against full GEANT4 simulation for several selected signal samples. All MC samples are produced with a varying number of simulated minimum-bias interactions overlaid on the hard-scattering event to account for multiple pp interactions in the same or nearby bunch crossing (pileup). The simulated events are reweighted to match the distribution in data. Corrections are applied to the simulated events to correct for differences between data and simulation for the lepton trigger and reconstruction efficiencies, momentum scale, energy resolution, isolation, and for the efficiency of identifying jets originating from the fragmentation of b -quarks, together with the probability for mis-tagging light-flavor and charm quarks.

5. Event and physics object reconstruction

Events are required to have a primary vertex [52] reconstructed from at least two associated tracks with $p_T > 400$ MeV and which are compatible with originating from the luminous region. If more than one such vertex is found, the vertex with the largest summed p_T^2 of the associated tracks is chosen.

Jets are reconstructed from three-dimensional topological clusters of noise-suppressed calorimeter cells [53] using the anti- k_t jet algorithm [54] with a distance parameter $R = 0.4$. An area-based correction is applied to account for energy from additional pp collisions based on an estimate of the pileup activity in a given event [55]. Calibrated [56] jets are required to have $p_T > 20$ GeV and $|\eta| < 2.8$. Events containing jets arising from non-collision sources or detector noise [57] are removed from consideration. Additional selections are applied to jets with $p_T < 60$ GeV and $|\eta| < 2.4$ to reject events that originate from pileup interactions [58].

Jets initiated by a b -quark and which are within the inner detector acceptance ($|\eta| < 2.5$) are identified with a multivariate algorithm that exploits the impact parameters of the charged-particle tracks, the presence of secondary vertices and the reconstructed flight paths of b - and c -hadrons inside the jet [59–61]. The average identification efficiency of jets containing b -quarks is 77% as measured with simulated $t\bar{t}$ events. A rejection factor of approximately 134 is reached for light-quark and gluon jets (depending on the p_T of the jet) and 6.2 for charm jets.

Electron candidates are reconstructed from energy clusters in the electromagnetic calorimeter that are matched to a track in the inner detector. They are required to have $|\eta| < 2.47$, $p_T > 7$ GeV and must pass a variant of the “very loose” likelihood-based selection. In the case where the separation between an electron candidate and a non- b -tagged (b -tagged) jet is $\Delta R < 0.2$ ⁴, the object is considered to be an electron (b -tagged jet). If the separation between an electron candidate and any jet satisfies $0.2 < \Delta R < 0.4$, the object is considered to be a jet. Muons are reconstructed from matching tracks in the inner detector and in the muon spectrometer and are required to have $|\eta| < 2.7$, $p_T > 6$ GeV. If the separation between a muon and any jet is $\Delta R < 0.4$, the muon is omitted.

The $\mathbf{p}_T^{\text{miss}}$ is the negative vector sum of the p_T of all selected and calibrated physics objects in the event. An extra term is added to account for soft energy in the event that is not associated to any of the selected objects. This soft term is calculated from inner detector tracks with $p_T > 400$ MeV matched to the primary vertex to make it more resilient to pileup contaminations [62]. The missing transverse momentum from the tracking system (denoted as $\mathbf{p}_T^{\text{miss,track}}$, with magnitude $E_T^{\text{miss,track}}$) is computed from the vector sum of

⁴ For the overlap removal, rapidity is used instead of pseudorapidity in the ΔR definition.

the reconstructed inner detector tracks with $p_T > 500$ MeV, $|\eta| < 2.5$, that are associated with the primary vertex in the event.

The requirements on electrons and muons are tightened for the selection of events in background control regions (described in section 7) containing leptons. Both electron and muon candidates are required to have $p_T > 20$ GeV and satisfy p_T -dependent track- and calorimeter-based isolation criteria. Electron and muon candidates matched to trigger electron (muon) candidates must have p_T exceeding the corresponding trigger threshold by at least 2 GeV. Electron candidates are required to pass a “tight” likelihood-based selection. The impact parameter of the electron in the transverse plane with respect to the reconstructed event primary vertex ($|d_0|$) is required to be less than five times the impact parameter uncertainty (σ_{d0}). The impact parameter along the beam direction, $|z_0 \times \sin \theta|$, is required to be less than 0.5 mm. Further selection criteria on reconstructed muons are also imposed: muon candidates are required to pass a “medium” quality selection [63]. In addition, the requirements $|d_0| < 3\sigma_{d0}$ and $|z_0 \times \sin \theta| < 0.5$ mm are imposed for muon candidates.

6. Signal region definitions

The main experimental signature for all signal topologies is the presence of multiple jets (two of which originate from b -quarks), no leptons, and significant missing transverse momentum.

A common preselection is defined for all signal regions. At least four jets are required, at least one of which must be b -tagged. The leading four jets must satisfy $p_T > 80, 80, 40, 40$ GeV. Events containing reconstructed electrons or muons are vetoed. The E_T^{miss} trigger dictates the requirement $E_T^{\text{miss}} > 250$ GeV and rejects the majority of background from multijet and all-hadronic $t\bar{t}$ events. In order to reject events with mis-measured E_T^{miss} originating from multijet and hadronic $t\bar{t}$ decays, an angular separation between the azimuthal angle of the two highest p_T jets and the E_T^{miss} is required: $|\Delta\phi(\text{jet}^{0,1}, E_T^{\text{miss}})| > 0.4$. Further reduction of such events is attained by requiring the $E_T^{\text{miss,track}}$ to be aligned in ϕ with respect to the E_T^{miss} calculated from the calorimeter system: $E_T^{\text{miss,track}} > 30$ GeV and $|\Delta\phi(E_T^{\text{miss}}, E_T^{\text{miss,track}})| < \pi/3$ radians.

Beyond these common requirements, six sets of signal regions (SRA-F) are defined to target each topology and kinematic regime. SRA (SRB) is sensitive to production of high-mass \tilde{t} pairs with large (small) $\Delta m(\tilde{t}, \tilde{\chi}^0)$. Both SRA and SRB employ top mass reconstruction techniques to reject background. SRC is targeted at $\tilde{t} \rightarrow b\tilde{\chi}_1^\pm$ decays, where no top quark candidates are reconstructed. SRD is designed for the highly compressed region with $\Delta m(\tilde{t}, \tilde{\chi}^0) \sim m_t$. In this signal region, initial state radiation (ISR) is used to improve sensitivity to these decays. SRE is aimed at dark matter + $t\bar{t}$ final states, and SRF is optimized for scenarios with highly boosted top quarks that can occur in gluino-mediated top squark production.

Signal Region Sets A and B

SRA and SRB are targeted at direct top squark pair production where the top squarks decay via $\tilde{t} \rightarrow t\tilde{\chi}_1^0$ and $\Delta m(\tilde{t}, \tilde{\chi}_1^0) > m_t$. SRA is optimized for $m_{\tilde{t}} = 800$ GeV, $m_{\tilde{\chi}^0} = 1$ GeV while SRB is optimized for $m_{\tilde{t}} = 600$ GeV, $m_{\tilde{\chi}^0} = 300$ GeV. Two b -tagged jets are required.

The decay products of the $t\bar{t}$ system in the all-hadronic decay mode can often be reconstructed as six distinct $R = 0.4$ jets. The transverse shape of these jets is typically circular with a radius equal to this distance parameter, but when two of the jets are less than $2R$ apart in $\eta - \phi$ space, the one-to-one correspondence

of a jet with a top daughter may no longer hold. Thus, the two hadronic top candidates are reconstructed by applying the anti- k_t clustering algorithm [54] to the $R = 0.4$ jets, using reclustered distance parameters of $R = 0.8$ and $R = 1.2$. Two $R = 1.2$ reclustered jets are required; the mass of the highest p_T $R = 1.2$ reclustered jet is shown in Fig. 2 (a). The events are divided into three categories based on the resulting $R = 1.2$ reclustered jet masses, as illustrated in Fig. 3: the “TT” category includes events with two well-reconstructed top candidates, the “TW” category contains events with one well-reconstructed top candidate and a well-reconstructed W candidate, and the “T0” category represents events with only one well-reconstructed top candidate. Since the signal-to-background ratio is quite different in each of these categories, they are optimized individually for both SRA and SRB.

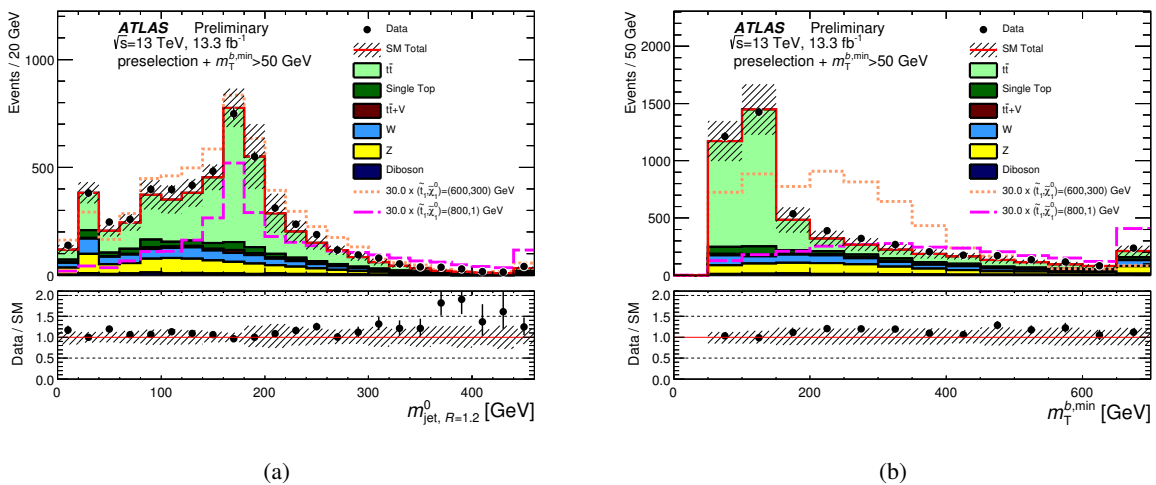


Figure 2: Distributions of discriminating variables after the common preselection and an additional $m_T^{b,\min} > 50$ GeV requirement. The stacked histograms show the SM expectation, normalized using scale factors derived from the simultaneous fit to all backgrounds. The “Data/SM” plots show the ratio of data events to the total SM expectation. The hatched uncertainty band around the SM expectation and in the ratio plots illustrates the combination of statistical and detector-related systematic uncertainties. The rightmost bin includes all overflows.

The most powerful discriminating variable against SM $t\bar{t}$ production is the E_T^{miss} resulting from the undetected $\tilde{\chi}_1^0$ s. Substantial $t\bar{t}$ background rejection is provided by additional requirements to reject events in which one W decays via a lepton plus neutrino. The first requirement is that the transverse mass (m_T) calculated from the E_T^{miss} and the b -tagged jet closest in ϕ to the $\mathbf{p}_T^{\text{miss}}$ direction is above 200 GeV:

$$m_T^{b,\min} = \sqrt{2 p_T^b E_T^{\text{miss}} [1 - \cos \Delta\phi (\mathbf{p}_T^b, \mathbf{p}_T^{\text{miss}})]} > 200 \text{ GeV}, \quad (1)$$

as illustrated in Fig. 2 (b). The second requirement is a “ τ -veto” targeted at hadronic τ lepton candidates likely to have originated from a $W \rightarrow \tau\nu$ decay. Events that contain a non- b -tagged jet within $|\eta| < 2.5$ with ≤ 4 associated charged-particle tracks with $p_T > 500$ MeV, and where the $\Delta\phi$ between the jet and the $\mathbf{p}_T^{\text{miss}}$ is less than $\pi/5$ radians, are vetoed. In SRB, additional discrimination is provided by $m_T^{b,\max}$ and $\Delta R(b, b)$. The former quantity is analogous to $m_T^{b,\min}$ except that the transverse mass is computed with the b -tagged jet that has the largest $\Delta\phi$ with respect to the $\mathbf{p}_T^{\text{miss}}$ direction. The latter quantity provides additional discrimination against background where the two b -tagged jets come from a gluon splitting. Table 1 summarizes the selection criteria that are used in these two signal regions.

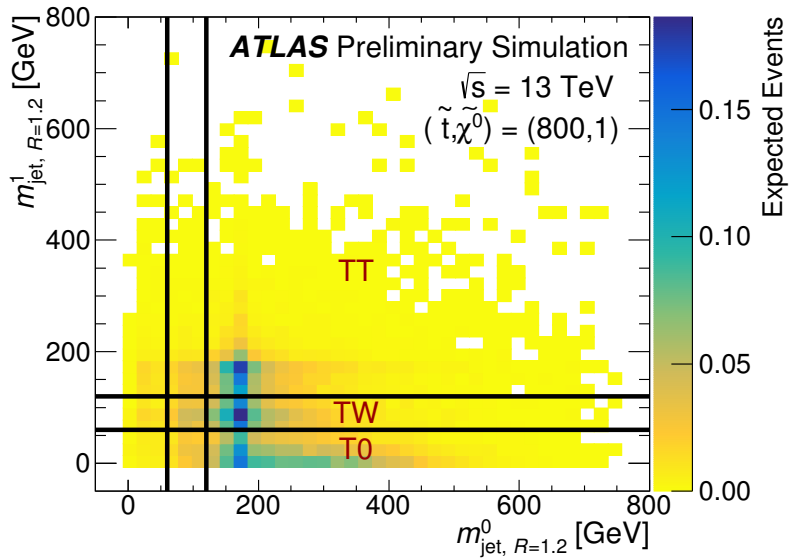


Figure 3: Illustration of signal region categories (TT, TW, and T0) based on the $R = 1.2$ reclustered top candidate masses for simulated direct top squark pair production with $(\tilde{t}, \tilde{\chi}_1^0) = (800, 1)$ GeV after the loose preselection requirement described in the text.

Signal Region Sets C

SRC is optimized for direct top squark pair production where both top squarks decay via $\tilde{t} \rightarrow b\tilde{\chi}_1^\pm$. In this signal region, at least four jets are required with $p_T > 150, 100, 40, 40$ GeV, two of which must be b -tagged. SRC-low, SRC-med, and SRC-high are optimized for $m_{\tilde{t}} = 400$ GeV, $m_{\tilde{\chi}_1^0} = 50$ GeV, $m_{\tilde{t}} = 600$ GeV, $m_{\tilde{\chi}_1^0} = 100$ GeV, and $m_{\tilde{t}} = 700$ GeV, $m_{\tilde{\chi}_1^0} = 50$ GeV, respectively. The models considered for the optimization have $m(\tilde{\chi}_1^\pm) = 2m(\tilde{\chi}_1^0)$. Tighter leading and sub-leading jet p_T requirements are made for SRC-med and SRC-high, as summarized in Table 2. Additional discrimination is provided by a measure of the E_T^{miss} significance: $E_T^{\text{miss}}/\sqrt{H_T}$, where H_T is the scalar sum of the p_T of all reconstructed $R = 0.4$ jets in an event. $E_T^{\text{miss}}/\sqrt{H_T} > 5\sqrt{\text{GeV}}$ is required, and an upper cut on this quantity of $12\sqrt{\text{GeV}}$ for the SRC-low and SRC-med regions and $17\sqrt{\text{GeV}}$ for the SRC-high region is applied.

The best sensitivity for this signal scenario is achieved by vetoing events with reconstructed top candidates. An alternative top reconstruction, with respect to the method used in the SRA and SRB selections, is used. The two jets with the highest weights from the b -tagging identification algorithm are selected. Among the remaining jets, the two closest in ΔR are combined to form a W candidate. The closest (in ΔR) high-weight b -tagged jet to this W candidate is then combined with it to form a top candidate. The mass of this resulting top candidate, m_{bjj} , is then required to be > 250 GeV, ensuring background rejection in the low m_{bjj} region. The high m_{bjj} region, above the top mass, characteristically has less background contamination while still having significant signal contributions.

Table 1: Selection criteria for SRA and SRB, in addition to the common preselection requirements described in the text. The signal regions are separated into topological categories based on reconstructed top candidate masses.

Signal Region		TT	TW	T0
	$m_{\text{jet}, R=1.2}^0$	$> 120 \text{ GeV}$	$> 120 \text{ GeV}$	$> 120 \text{ GeV}$
	$m_{\text{jet}, R=1.2}^1$	$> 120 \text{ GeV}$	$60 - 120 \text{ GeV}$	$< 60 \text{ GeV}$
SRA	$m_{\text{jet}, R=0.8}^0$	$> 60 \text{ GeV}$		
	b -tagged jets	≥ 2		
	$m_T^{b, \text{min}}$	$> 200 \text{ GeV}$		
	τ -veto	yes		
	E_T^{miss}	$> 400 \text{ GeV}$	$> 450 \text{ GeV}$	$> 500 \text{ GeV}$
SRB	b -tagged jets	≥ 2		
	$m_T^{b, \text{min}}$	$> 200 \text{ GeV}$		
	$m_T^{b, \text{max}}$	$> 200 \text{ GeV}$		
	τ -veto	yes		
	$\Delta R(b, b)$	> 1.2		
	E_T^{miss}	$> 250 \text{ GeV}$		

Table 2: Selection criteria for SRC, in addition to the common preselection requirements described in the text.

Variable	SRC-low	SRC-med	SRC-high
$m_{b jj}$	$> 250 \text{ GeV}$		
b -tagged jets	≥ 2		
p_T^0	$> 150 \text{ GeV}$	$> 200 \text{ GeV}$	$> 250 \text{ GeV}$
p_T^1	$> 100 \text{ GeV}$	$> 150 \text{ GeV}$	$> 150 \text{ GeV}$
$m_T^{b, \text{min}}$	$> 250 \text{ GeV}$	$> 300 \text{ GeV}$	$> 350 \text{ GeV}$
$m_T^{b, \text{max}}$	$> 350 \text{ GeV}$	$> 450 \text{ GeV}$	$> 500 \text{ GeV}$
$\Delta R(b, b)$	> 0.8		
$E_T^{\text{miss}} / \sqrt{H_T}$	$[5, 12] \sqrt{\text{GeV}}$	$[5, 12] \sqrt{\text{GeV}}$	$[5, 17] \sqrt{\text{GeV}}$
E_T^{miss}	$> 250 \text{ GeV}$		

Signal Region Sets D

SRD is optimized for direct top squark pair production where $\Delta m(\tilde{t}, \tilde{\chi}_1^0) \sim m_t$, a regime in which the signal topology is extremely similar to SM $t\bar{t}$ production. However, in the presence of high-momentum ISR, the di-top-squark system is boosted in the transverse plane. The ratio of the E_T^{miss} to the p_T of the ISR system in the CM frame (p_T^{ISR}), defined as R_{ISR} , is proportional to the ratio of the $\tilde{\chi}_1^0$ and \tilde{t} masses [64, 65]:

$$R_{\text{ISR}} \equiv \frac{E_T^{\text{miss}}}{p_T^{\text{ISR}}} \sim \frac{m_{\tilde{\chi}_1^0}}{m_{\tilde{t}}}. \quad (2)$$

A recursive jigsaw reconstruction technique, as described in Ref. [66], is used to divide each event into an ISR hemisphere and a sparticle hemisphere, where the latter consists of the pair of candidate top squarks, each of which decays via a top quark and $\tilde{\chi}_1^0$. Objects are grouped together based on their proximity in the lab frame's transverse plane by minimizing the reconstructed transverse masses of the ISR system and sparticle system simultaneously over all choices of object assignment. Kinematic variables are then defined based on this assignment of objects to either the ISR system or the sparticle system.

The selection criteria for this signal region are summarized in Table 3. The events are divided into eight windows defined by overlapping ranges of the reconstructed R_{ISR} , and target different top squark and $\tilde{\chi}_1^0$ masses: e.g., SRD1 is optimized for $m_{\tilde{t}} = 250$ GeV, $m_{\tilde{\chi}_1^0} = 77$ GeV and SRD5 is optimized for $m_{\tilde{t}} = 450$ GeV, $m_{\tilde{\chi}_1^0} = 277$ GeV. Five jets or more are required to be assigned to the sparticle hemisphere of the event, and at least one (two) of those jets must be b -tagged in SRD1-4 (SRD5-8). Transverse momentum requirements on p_T^{ISR} , the highest- p_T b -jet in the sparticle hemisphere ($p_T^{b\text{-tag},S}$), and the fourth-highest- p_T jet in the sparticle hemisphere ($p_T^{\text{jet}4,S}$) are applied. The transverse mass between the sparticle system and the E_T^{miss} , defined as M_T^S , is required to be > 300 GeV. The ISR system is also required to be separated in azimuth from the E_T^{miss} in the CM frame; this variable is defined as $\Delta\phi_{\text{ISR}}$.

Table 3: Selection criteria for SRD, in addition to the common preselection requirements described in the text. The signal regions are separated into windows based on ranges of R_{ISR} .

Variable	SRD1	SRD2	SRD3	SRD4	SRD5	SRD6	SRD7	SRD8
min R_{ISR}	0.25	0.30	0.35	0.40	0.45	0.50	0.55	0.60
max R_{ISR}	0.40	0.45	0.50	0.55	0.60	0.65	0.70	0.75
b -tagged jets	≥ 2				≥ 1			
N_{jet}^S					≥ 5			
p_T^{ISR}					> 400 GeV			
$p_T^{b\text{-tag},S}$					> 40 GeV			
$p_T^{\text{jet}4,S}$					> 50 GeV			
M_T^S					> 300 GeV			
$\Delta\phi_{\text{ISR}}$					> 3.0 radians			

Signal Region E

SRE is targeted at signal models of the associated production of top pairs with a pair of dark matter particles produced through a scalar (pseudoscalar) mediator φ (a) as illustrated in Fig. 1(e). Four or more reconstructed jets are required, two of which must be b -tagged. The discriminating variables considered have been described previously for SRA, SRB and SRC, but a dedicated optimization is performed using the $m_\varphi = 350$ GeV, $m_\chi = 1$ GeV simplified model as a benchmark. The resulting selection criteria are summarized in Table 4.

Signal Region F

SRF is designed for models which have highly boosted top quarks. Such signatures can arise from direct pair production of high-mass top partners, or from the gluino-mediated compressed \tilde{t} scenario with large $\Delta m(\tilde{g}, \tilde{t})$ as illustrated in Fig. 1(d). Four or more reconstructed jets are required, two of which must be b -tagged. In this regime, reclustered jets with $R = 0.8$ are utilized to optimize experimental sensitivity to these highly boosted top quarks. The selection criteria for SRF, optimized for $m_{\tilde{g}} = 1400$ GeV, $m_{\tilde{t}} = 400$ GeV, $m_{\tilde{\chi}^0} = 395$ GeV, are summarized in Table 4.

Table 4: Selection criteria for SRE and SRF, in addition to the common preselection requirements described in the text.

Variable	SRE	SRF
b -tagged jets	≥ 2	
$m_{\text{jet}, R=1.2}^0$	> 140 GeV	-
$m_{\text{jet}, R=1.2}^1$	> 60 GeV	-
$m_{\text{jet}, R=0.8}^0$	-	> 120 GeV
$m_{\text{jet}, R=0.8}^1$	-	> 60 GeV
$m_T^{b, \text{min}}$	> 200 GeV	> 175 GeV
τ -veto	yes	no
$\Delta R(b, b)$	> 1.5	-
E_T^{miss}	> 300 GeV	> 250 GeV
H_T	-	> 1100 GeV
$E_T^{\text{miss}}/\sqrt{H_T}$	$> 14\sqrt{\text{GeV}}$	$> 15\sqrt{\text{GeV}}$

7. Background estimation

The main SM background process in SRA–C, E, and F is $Z \rightarrow \nu\bar{\nu}$ production in association with heavy flavor jets. The second most dominant background is $t\bar{t}$ production where one W decays via a lepton and neutrino and the lepton (particularly a hadronically decaying τ lepton) is either not identified or is reconstructed as a jet. This process is the major background contribution in SRD and an important background in SRB, SRC and SRE as well. Other important background processes are $W \rightarrow \ell\nu$ plus heavy flavor jets, single top and the irreducible background from $t\bar{t} + Z$, where the Z decays to two neutrinos.

The main background contributions are estimated primarily from comparisons between data and simulation. Control regions (CRs) are designed to enhance a particular source of background, and are orthogonal to the SRs while probing a similar event topology. The CRs are used to normalize the simulation to data, but the shape and extrapolation from the CR to the SR are taken from simulation. Sufficient data are needed to avoid large statistical uncertainties in the background estimates, and the CR definitions are chosen to be kinematically as close as possible to all SRs, to minimize the systematic uncertainties associated with extrapolating the background yield from the CR to the SR. Where CR definitions are farther from the SR definition, validation regions are employed to cross-check the extrapolation. In addition, control region selection criteria are chosen to minimize potential contamination from signal in the scenarios considered. The signal contamination is below 16% in all CRs for all signal benchmark points that have not been excluded by Run 1 searches. As the CRs are not 100% pure in the process of interest, the cross-contamination between CRs from other processes is estimated with simulated samples. The normalization factors and the cross contamination are determined simultaneously for all regions using a fit described below.

Table 5 details the relative contribution for each SM background process as a function of the signal region, as well as the corresponding control region used to estimate that background contribution. Each control region may serve to estimate backgrounds from several signal regions. Normalization scale factors (SFs) for each background source are also presented.

Detailed CR definitions are given in Table 6, and are defined by the presence of one or more leptons that make them orthogonal with the signal regions. The $|\Delta\phi(\text{jet}^{0,1}, E_T^{\text{miss}})|$, minimum $m_T(\ell, E_T^{\text{miss}})$, and $m_{\text{jet},R=1.2}^0$ requirements are designed to remove contamination from SM multijet processes (when defining these variables, only true jets are used, i.e. not the lepton). The number of leptons is indicated by N_ℓ and the transverse momentum of the lepton is indicated by p_T^ℓ . In all one-lepton CRs, once the trigger and minimum p_T^ℓ selection are applied, the lepton is treated as a non- b -tagged jet (as a stand-in for the hadronic τ leptons in the SRs) in the computation of all jet-related variables. In the two-lepton CRZ, the invariant mass of the two oppositely charged leptons, indicated by $m_{\ell\ell}$, is selected to be consistent with the leptons having originated from a Z . These leptons are then vectorially added to the E_T^{miss} to mimic the $Z \rightarrow \nu\bar{\nu}$ decays in the SRs, forming the quantity $E_T^{\text{miss}'}$. Requirements such as the maximum $m_T(\ell, E_T^{\text{miss}})$ and the minimum ΔR between the two highest-weight b -tagged jets and the lepton, $\Delta R(b, \ell)_{\text{min}}$, are used to enforce orthogonality. In CRST, the requirement on the invariant mass of the two highest-weight b -tagged jets, m_{bb} , is used to reject $t\bar{t}$ contamination from the control region enriched in single-top events. Distributions from the $Z + \text{jets}$ and $W + \text{jets}$ control regions (CRZ and CRW, respectively) are shown in Fig. 4, while Fig. 5 contains distributions from the $t\bar{t}$ and single top quark control regions (CRT and CRT-ISR, and CRST, respectively).

Contributions from all-hadronic $t\bar{t}$ and multijet production are found to be negligible. These are estimated from data using a procedure described in detail in Ref. [67]. The procedure determines the jet response from simulated dijet events, and then uses this response function to smear the jet response in low- E_T^{miss}

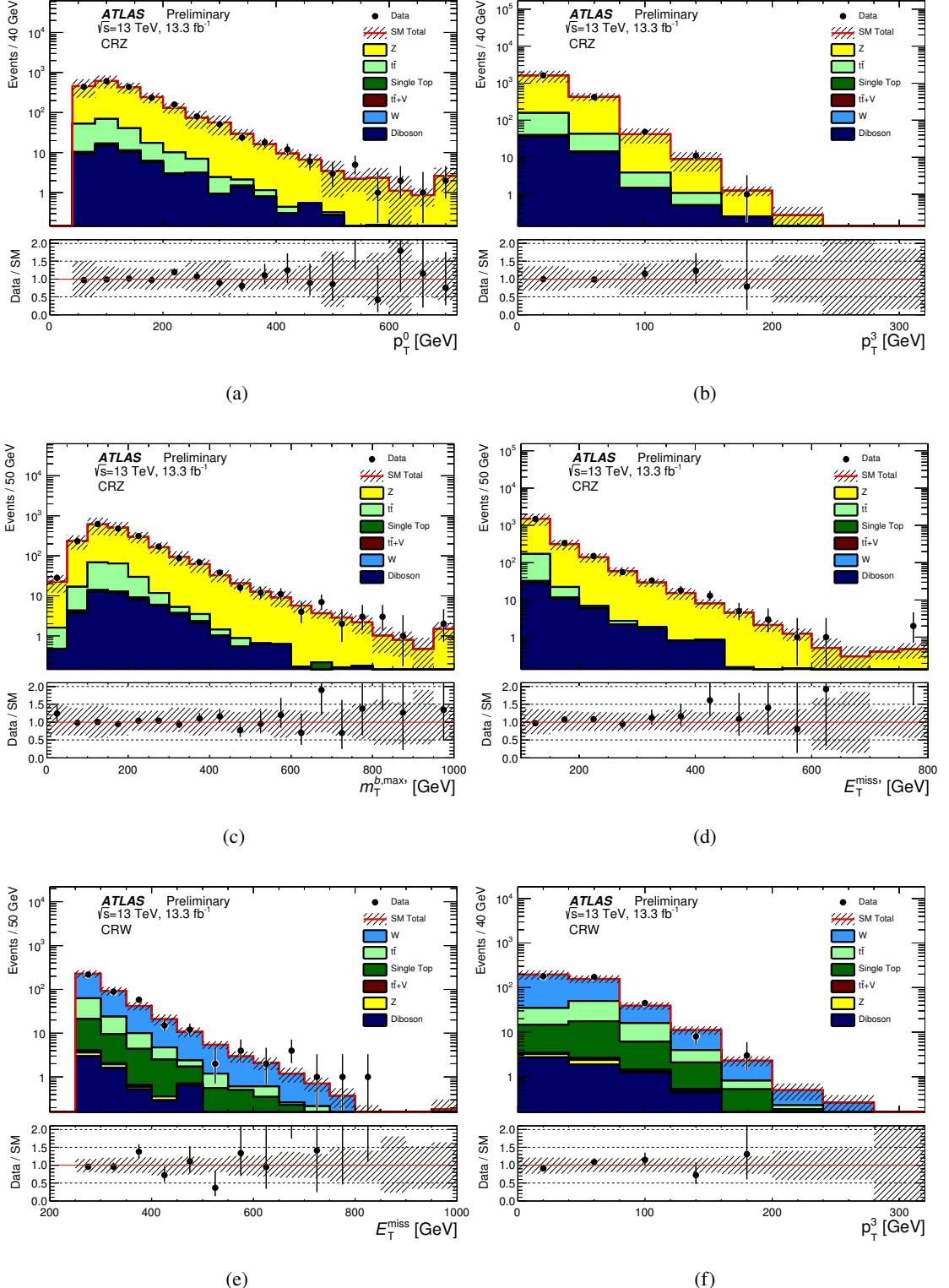


Figure 4: Transverse momenta of (a) the leading- p_T jet, (b) the fourth-leading- p_T jet, (c) the $m_T^{b,\text{max}'}$ distribution, and (d) the $E_T^{\text{miss}'}$ distribution in CRZ, and (e) the E_T^{miss} and (f) the transverse momentum of the fourth-leading- p_T jet in CRW. The stacked histograms show the SM expectation, normalized using scale factors derived from the simultaneous fit to all backgrounds. The “Data/SM” plots show the ratio of data events to the total SM expectation. The hatched uncertainty band around the SM expectation and in the ratio plot illustrates the combination of MC statistical and detector-related systematic uncertainties. The rightmost bin includes all overflows.

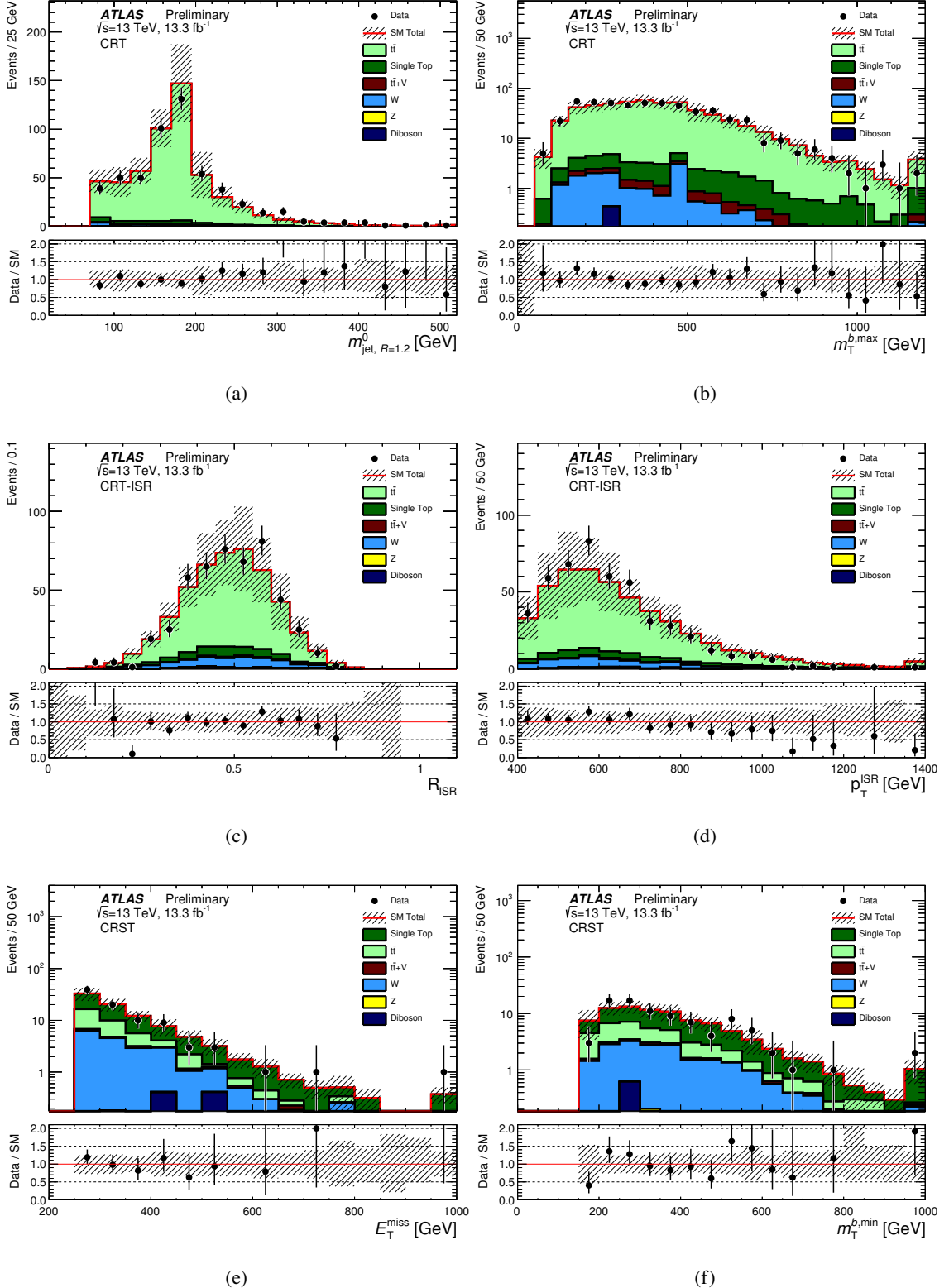


Figure 5: Distributions of (a) $m_{\text{jet}, R=1.2}^0$ and (b) $m_T^{b,\text{max}}$ in CRT, (c) R_{ISR} and (d) p_T^{ISR} in CRT-ISR, and (e) E_T^{miss} and (f) $m_T^{b,\text{min}}$ in CRST. The stacked histograms show the SM expectation, normalized using scale factors derived from the simultaneous fit to all backgrounds. The “Data/SM” plots show the ratio of data events to the total SM expectation. The hatched uncertainty band around the SM expectation and in the ratio plots illustrates the combination of MC statistical and detector-related systematic uncertainties. The rightmost bin includes all overflows.

Table 5: Summary of control regions used to estimate the background contributions for each signal region. The percentages indicate the relative contribution of each background process; for example, SRA contains predominantly $Z + \text{jets}$ and the normalization of the simulation is determined by data-MC comparison in CRZ. The ranges in percentages correspond to the variation across the signal subregions. The contributions may not total 100% since sub-dominant background contributions from $t\bar{t} + W/Z$, diboson, all-hadronic $t\bar{t}$, and multijet processes are not listed. Normalization scale factors (SF) for each CR calculated from a simultaneous fit (described in 7) to all backgrounds in all the CRs are also presented; the given uncertainty is the combination of the corresponding MC statistical and detector-related systematic uncertainties.

	$Z + \text{jets}$	$t\bar{t}$		$W + \text{jets}$	single top
	CRZ	CRT	CRT-ISR	CRW	CRST
SF	1.20 ± 0.26	0.91 ± 0.18	0.78 ± 0.19	1.21 ± 0.21	0.86 ± 0.33
SRA	34%-58%	9%-14%	-	10%-11%	6%-9%
SRB	22%-42%	22%-25%	-	9%-13%	10%
SRC	37%-39%	6%-17%	-	18%-25%	20%-26%
SRD1-4	0%	-	91%-92%	2%	1%-4%
SRD5-8	2%-10%	-	70%-84%	5%-9%	4%-8%
SRE	38%	12%	-	8%	10%
SRF	32%	10%	-	12%	17%

seed events. The jet response is cross-checked with data where the E_T^{miss} can be unambiguously attributed to the mis-measurement of one of the jets. Diboson and $t\bar{t} + W/Z$ production, which is also sub-dominant, is estimated directly from simulation.

Simultaneous fit to determine SM background

The observed numbers of events in the various control regions are included in a profile likelihood fit [68] to determine the SM background estimates in each signal region. A likelihood function is built as the product of Poisson probability functions, describing the observed and expected number of events in the control regions [69]. This procedure takes common systematic uncertainties (discussed in detail in Section 8) between the control and signal regions and their correlations into account; they are treated as nuisance parameters in the fit and are modelled by Gaussian probability density functions. The free parameters in the fit are the overall normalizations of the backgrounds listed in Table 5. The contributions from all other background processes are fixed at the values expected from the simulation, using the most accurate theoretical cross sections available, as described in Section 4.

The background estimates are validated by predicting the background in dedicated regions and comparing to observation. Validation regions are designed to be orthogonal to the control and signal regions while retaining kinematics and event composition close to the SRs but with little contribution from signal in any of the models considered. The $Z + \text{jets}$ validation region are designed slightly differently in that they are subsets of the $Z + \text{jets}$ control region which are still orthogonal to the signal regions.

Table 6: Selection criteria for the control regions used to estimate the background contributions in the signal regions.

Selection	CRZ	CRT	CRT-ISR	CRST	CRW
Trigger	electron (muon)			E_T^{miss}	
N_ℓ	2			1	
p_T^ℓ				$> 20 \text{ GeV}$	
$m_{\ell\ell}$	[86,96] GeV			-	
N_{jet}	≥ 4			≥ 4 (including leptons)	
jet p_T	(40, 40, 20, 20) GeV		(80, 80, 40, 40) GeV		(80, 80, 20, 20) GeV
E_T^{miss}	$< 50 \text{ GeV}$			$> 250 \text{ GeV}$	
$E_T^{\text{miss}'}$	$> 70 \text{ GeV}$			-	
b -tagged jets	≥ 2	≥ 2	≥ 1	≥ 2	$= 1$
$ \Delta\phi(\text{jet}^{0,1}, E_T^{\text{miss}}) $	-			> 0.4	
$\min m_T(\ell, E_T^{\text{miss}})$	-	30 GeV	-	30 GeV	30 GeV
$\max m_T(\ell, E_T^{\text{miss}})$	-	120 GeV	80 GeV	120 GeV	100 GeV
$m_{\text{jet}, R=1.2}^0$	-	$> 70 \text{ GeV}$	-	$> 70 \text{ GeV}$	$< 60 \text{ GeV}$
$m_T^{b,\text{min}}$	-	$> 100 \text{ GeV}$	-	$> 175 \text{ GeV}$	-
$\Delta R(b, \ell)_{\text{min}}$	-	< 1.5	< 2.0	> 1.5	> 2.0
m_{bb}	-	-	-	$> 200 \text{ GeV}$	-
N_{jet}^S	-	-	≥ 5	-	-
$N_{b\text{-tag}}^S$	-	-	≥ 1	-	-
p_T^{ISR}	-	-	$\geq 400 \text{ GeV}$	-	-

8. Systematic uncertainties

Several sources of experimental and theoretical systematic uncertainties are considered in the SM background estimates and signal expectations and are included in the profile likelihood fit described in Section 7.

The dominant uncertainty to all SRs except for SRB-T0 is the statistical uncertainty on the mean estimate of the total background contribution. The main sources of detector-related systematic uncertainties in the SM background estimates originate from the jet energy scale (JES) and resolution (JER). The effect of the JES uncertainty on the background estimates in the signal regions is 1-4% in SRA and SRB, 1-5% in SRC, 2-9% in SRD, 5% in SRE and 2% in SRF. The uncertainty on the b -tagging efficiency has a large contribution as well. Its effect is 1-5% in SRA, 1-3% in SRB, 1-8% in SRC, 1-4% in SRD and is about 12% for SRE and 23% for SRF. Lepton reconstruction and identification uncertainties are also considered but have a small impact. All jet- and lepton-related uncertainties are propagated to the calculation of the E_T^{miss} , and additional uncertainties on the energy and resolution of the soft term are also included. The uncertainty on the soft term of the E_T^{miss} is most significant in SRD ranging between 1 and 10%, while being about 7% in both SRE and SRF. An uncertainty due to the pileup is also considered with a contribution in SRA of 1-6%, in SRB of 1-3%, in SRC of 1-2%, in SRD of 2-15%, in SRE of 3% and in SRF of 10%.

A 2.9% uncertainty in the luminosity measurement is also taken into consideration for all signal and background estimates that are directly derived from MC simulations.

Theoretical uncertainties in the modelling of the SM background are evaluated. For the $W/Z + \text{jets}$ background processes, the modelling uncertainties are evaluated using SHERPA samples varying the renormalization and factorization scales, and the merging (CKKW) and resummation scales. The resulting impact on the total background yields from the $Z + \text{jets}$ ($W + \text{jets}$) theoretical uncertainties are 7-12% (2%) for SRA, 4-9% (1-3%) for SRB, 8% (2-3%) for SRC, less than 1% for SRD, 8% (1%) for SRE and 7% (2%) for SRF.

For the $t\bar{t}$ background, uncertainties are evaluated due to the hard scattering generation (comparing **MADGRAPH5AMC@NLO** with **POWHEG-Box**), the choice of the parton showering model (**PYTHIA** vs. **HERWIG++**) and the emission of additional partons in the initial and final states [46]. The largest impact of the $t\bar{t}$ systematics on the total background yields arises for SRD and is about 22%, with lower contributions to SRC of 10%. For $t\bar{t}+W/Z$ background, the theoretical uncertainty is dominated by the 13% uncertainty on the production cross section. Additional variations considered include the choice of renormalization and factorization scales (each varied up and down by a factor of two). Uncertainty due to the choice of the generator is also considered comparing SHERPA at NLO with **MADGRAPH5AMC@NLO**. The single top background is dominated by the Wt subprocess. Uncertainties are evaluated for the choice of the parton showering model (**PYTHIA** vs. **HERWIG++**) and for the emission of additional partons in the initial and final state radiation. These uncertainties are about 10% in SRA and SRB, 17-25% in SRC, 10% in SRE and 16% in SRF. A 100% uncertainty is applied to account for the effect of interference between single-top quark and $t\bar{t}$ production.

Finally, signal systematic uncertainties due to detector and acceptance effects are taken into account when setting limits. The main sources of these uncertainties are the JER, ranging from 3 to 23%, the JES, ranging from 6 to 16% and pile-up, ranging from 6 to 20%. The uncertainty on the estimated number of signal events that arises from the cross section uncertainties for the various processes is taken into account by calculating two additional limits considering a $\pm 1\sigma$ change in cross section. The cross section

uncertainty is $\sim 15\%$ for direct top squark production, $\sim 30\%$ for $t\bar{t}$ production in association with two DM particles, and $\sim 20\%$ for gluino production.

9. Results and interpretation

The observed event yields in data are compared to the total number of expected background events in Tables 7, 8, 9, 10, and 11. The total background estimate is determined from the simultaneous fit based on a procedure described in Section 7. Figure 6 illustrates the distribution of the E_T^{miss} and $m_T^{b,\text{max}}$ combining the categories of SRA and SRB, respectively. The distribution of $m_T^{b,\text{max}}$ in the most inclusive region of SRC, SRC-low, is shown in Fig. 7, while R_{ISR} is shown for the combined region of SRD1–4 and SRD5–8 in Fig. 8. Finally, the $E_T^{\text{miss}}/\sqrt{H_T}$ and H_T distributions for SRE and SRF, respectively, are presented in Fig. 9. In these figures, the background expectations are normalized to the values determined from the simultaneous fit.

Table 7: Expected and observed yields for SRA for $\int \mathcal{L} dt = 13.3 \text{ fb}^{-1}$.

	SRA-TT	SRA-TW	SRA-T0
Observed	8	5	16
Total SM	5.2 ± 1.4	5.7 ± 1.6	11.3 ± 2.6
$t\bar{t}$	$0.78^{+0.84}_{-0.78}$	0.60 ± 0.34	1.13 ± 0.79
$W + \text{jets}$	0.48 ± 0.19	0.54 ± 0.18	1.13 ± 0.31
$Z + \text{jets}$	1.83 ± 0.55	3.0 ± 1.2	6.7 ± 2.1
$t\bar{t}+W/Z$	1.03 ± 0.33	0.84 ± 0.26	1.29 ± 0.57
Single top	$0.45^{+0.53}_{-0.45}$	$0.34^{+0.40}_{-0.34}$	$0.88^{+0.97}_{-0.88}$
Dibosons	0.62 ± 0.44	0.31 ± 0.20	0.18 ± 0.14
Multijets	$0.02^{+0.05}_{-0.02}$	$0.01^{+0.02}_{-0.01}$	$0.02^{+0.05}_{-0.02}$

No significant excess above the SM expectation is observed in any of the signal regions; the p -values, which express the probability that the background fluctuates to the data or above, and the model independent limits are shown in Table 12. The smallest p -values are 8%, 10%, and 13% for SRB-TT, SRC-low, and SRB-T0, respectively. In cases where the data fluctuate below the background the p -value is equal to 0.50 (e.g. SRD8). The 95% confidence level (CL) upper limits on the number of beyond-the-SM (BSM) events in each signal region are derived using the CL_s prescription [70, 71] and calculated from asymptotic formulae [68]. Model-independent limits on the visible BSM cross sections, defined as $\sigma_{\text{vis}} = \sigma \cdot A \cdot \epsilon$, where σ is the production cross section, A is the acceptance, and ϵ is the selection efficiency for a BSM signal, are reported. In addition to the individual p -values of each signal region, combined p -values of 0.10 for both SRA and SRB are evaluated assuming the signal shape across categories of $m_{\tilde{t}} = 800 \text{ GeV}$, $m_{\tilde{\chi}^0} = 1 \text{ GeV}$ and $m_{\tilde{t}} = 600 \text{ GeV}$, $m_{\tilde{\chi}^0} = 300 \text{ GeV}$, respectively.

The detector acceptance multiplied by the efficiency ($A \cdot \epsilon$) is calculated for several signal regions and their benchmark points. The $A \cdot \epsilon$ for signal regions aimed at high energy final states, SRA, SRE, SRF, ranges between 4.1% and 6.5% for their respective signal benchmark points of $m_{\tilde{t}} = 800 \text{ GeV}$, $m_{\tilde{\chi}^0} = 1 \text{ GeV}$,

Table 8: Expected and observed yields for SRB for $\int \mathcal{L} dt = 13.3 \text{ fb}^{-1}$.

	SRB-TT		SRB-TW		SRB-T0	
Observed	17		18		84	
Total SM	10.6 \pm 2.3		16.7 \pm 3.6		60 \pm 14	
$t\bar{t}$	2.5 \pm 1.5		4.4 \pm 2.6		14.7 \pm 4.4	
$W + \text{jets}$	1.33 \pm 0.35		1.44 \pm 0.46		6.2 \pm 1.5	
$Z + \text{jets}$	2.40 \pm 0.70		5.1 \pm 1.6		26.0 \pm 8.8	
$t\bar{t}+W/Z$	2.51 \pm 0.64		3.15 \pm 0.79		6.0 \pm 1.4	
Single top	1.1 $^{+1.2}_{-1.1}$		1.7 $^{+1.9}_{-1.7}$		6.1 $^{+6.7}_{-6.1}$	
Dibosons	0.70 \pm 0.44		0.87 $^{+0.96}_{-0.87}$		1.33 \pm 0.75	
Multijets	0.06 $^{+0.13}_{-0.06}$		0.04 $^{+0.08}_{-0.04}$		0.14 $^{+0.29}_{-0.14}$	

Table 9: Expected and observed yields for SRC, SRE, and SRF for $\int \mathcal{L} dt = 13.3 \text{ fb}^{-1}$.

	SRC-low	SRC-med	SRC-high	SRE	SRF
Observed	36	14	9	9	3
Total SM	23.9 \pm 7.5	9.4 \pm 3.5	10.5 \pm 3.7	7.1 \pm 1.8	2.8 \pm 1.0
$t\bar{t}$	4.4 \pm 3.3	1.4 \pm 1.3	0.72 \pm 0.54	0.92 \pm 0.48	0.32 \pm 0.29
$W + \text{jets}$	4.4 \pm 1.3	1.85 \pm 0.69	2.51 \pm 0.57	0.56 \pm 0.17	0.33 \pm 0.12
$Z + \text{jets}$	9.5 \pm 3.7	3.5 \pm 1.6	4.0 \pm 1.4	2.78 \pm 0.98	0.92 \pm 0.52
$t\bar{t}+W/Z$	0.60 \pm 0.21	0.19 \pm 0.10	0.32 \pm 0.14	1.46 \pm 0.55	0.28 \pm 0.11
Single top	4.5 $^{+4.9}_{-4.5}$	2.3 $^{+2.5}_{-2.3}$	2.7 $^{+3.1}_{-2.7}$	0.70 $^{+0.80}_{-0.70}$	0.46 $^{+0.55}_{-0.46}$
Dibosons	0.44 $^{+0.66}_{-0.44}$	0.07 \pm 0.07	0.13 $^{+0.30}_{-0.13}$	0.63 \pm 0.48	0.50 \pm 0.31
Multijets	0.09 $^{+0.19}_{-0.09}$	0.05 $^{+0.11}_{-0.05}$	0.04 $^{+0.08}_{-0.04}$	0.01 $^{+0.02}_{-0.01}$	0.01 $^{+0.02}_{-0.01}$

Table 10: Expected and observed yields for SRD for $\int \mathcal{L} dt = 13.3 \text{ fb}^{-1}$.

	SRD1	SRD2	SRD3	SRD4
Observed	4	5	9	9
Total SM	4.3 \pm 1.9	7.1 \pm 3.2	8.8 \pm 3.4	9.4 \pm 3.7
$t\bar{t}$	3.9 \pm 1.9	6.5 \pm 3.3	8.0 \pm 3.4	8.5 \pm 3.8
$W + \text{jets}$	0.14 $^{+0.25}_{-0.14}$	0.18 $^{+0.27}_{-0.18}$	0.24 $^{+0.31}_{-0.24}$	0.26 \pm 0.20
$Z + \text{jets}$	0.04 \pm 0.02	0.06 \pm 0.03	0.08 \pm 0.06	0.08 $^{+0.28}_{-0.08}$
$t\bar{t}+W/Z$	0.11 \pm 0.08	0.16 \pm 0.12	0.20 \pm 0.10	0.15 \pm 0.13
Single top	0.09 $^{+0.14}_{-0.09}$	0.19 $^{+0.29}_{-0.19}$	0.29 $^{+0.57}_{-0.29}$	0.42 $^{+0.54}_{-0.42}$
Dibosons	--	--	--	--
Multijets	0.04 $^{+0.08}_{-0.04}$	0.04 $^{+0.08}_{-0.04}$	0.03 $^{+0.06}_{-0.03}$	0.02 $^{+0.04}_{-0.02}$

Table 11: Expected and observed yields for SRD for $\int \mathcal{L} dt = 13.3 \text{ fb}^{-1}$.

	SRD5	SRD6	SRD7	SRD8
Observed	11	6	5	1
Total SM	11.6 \pm 3.6	8.6 \pm 3.5	5.2 \pm 2.1	2.56 \pm 0.86
$t\bar{t}$	9.7 \pm 3.7	6.8 \pm 3.5	4.0 \pm 2.0	1.77 \pm 0.67
$W + \text{jets}$	0.68 \pm 0.40	0.68 \pm 0.23	0.37 \pm 0.22	0.25 \pm 0.18
$Z + \text{jets}$	0.27 $^{+0.52}_{-0.27}$	0.23 $^{+0.43}_{-0.23}$	0.36 \pm 0.13	0.30 \pm 0.13
$t\bar{t}+W/Z$	0.26 \pm 0.06	0.16 \pm 0.11	0.08 $^{+0.09}_{-0.08}$	0.02 $^{+0.02}_{-0.02}$
Single top	0.54 $^{+0.64}_{-0.54}$	0.48 $^{+0.56}_{-0.48}$	0.31 $^{+0.35}_{-0.31}$	0.22 $^{+0.25}_{-0.22}$
Dibosons	0.16 \pm 0.13	0.16 \pm 0.11	0.16 \pm 0.14	--
Multijets	0.03 $^{+0.06}_{-0.03}$	0.02 $^{+0.03}_{-0.02}$	0.01 $^{+0.01}_{-0.01}$	--

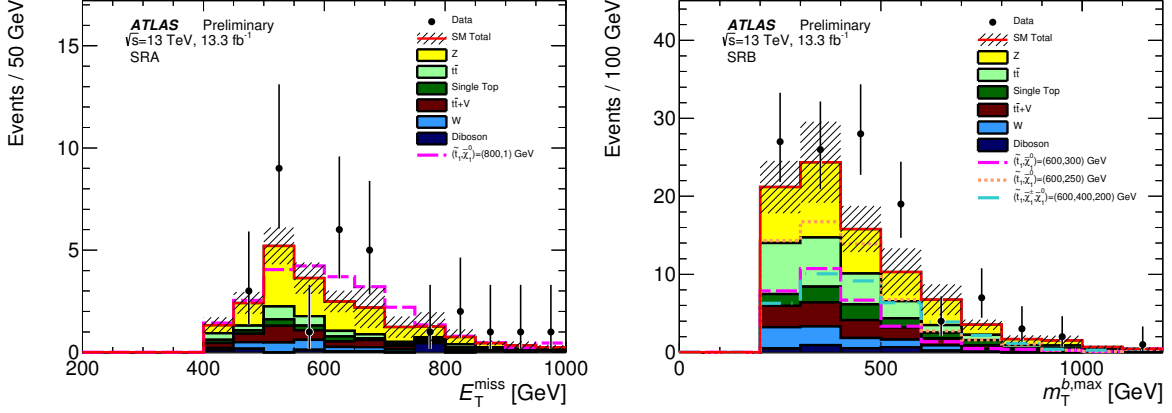


Figure 6: Distributions of E_T^{miss} for SRA and $m_T^{b,\text{max}}$ for SRB. The categories have been combined in these distributions. The stacked histograms show the SM expectation and the hatched uncertainty band around the SM expectation shows the MC statistical and detector-related systematic uncertainties.

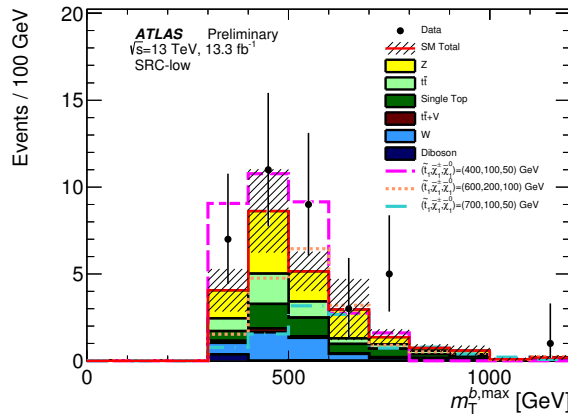


Figure 7: Distribution of $m_T^{b,\text{max}}$ in SRC-low. The stacked histograms show the SM expectation and the hatched uncertainty band around the SM expectation shows the MC statistical and detector-related systematic uncertainties.

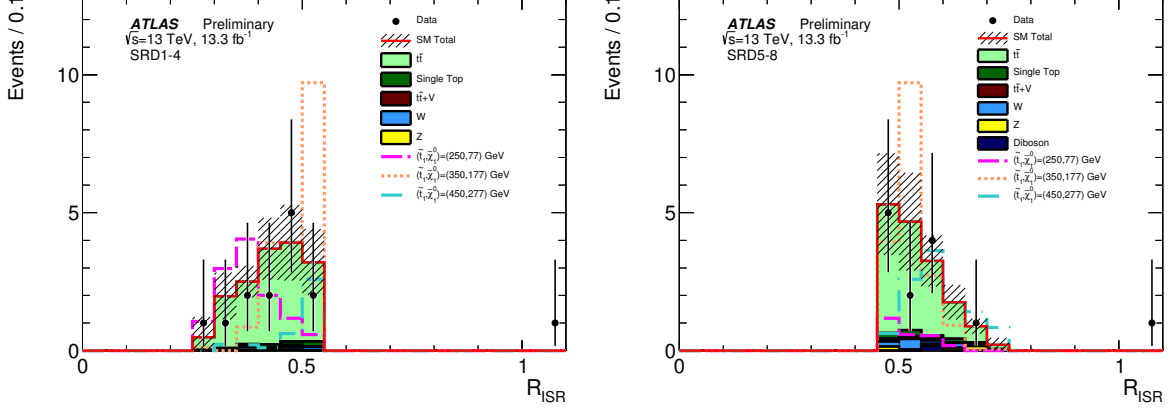


Figure 8: Distributions of R_{ISR} for SRD1-SRD4 and SRD5-SRD8. The stacked histograms show the SM expectation and the hatched uncertainty band around the SM expectation shows the MC statistical and detector-related systematic uncertainties.

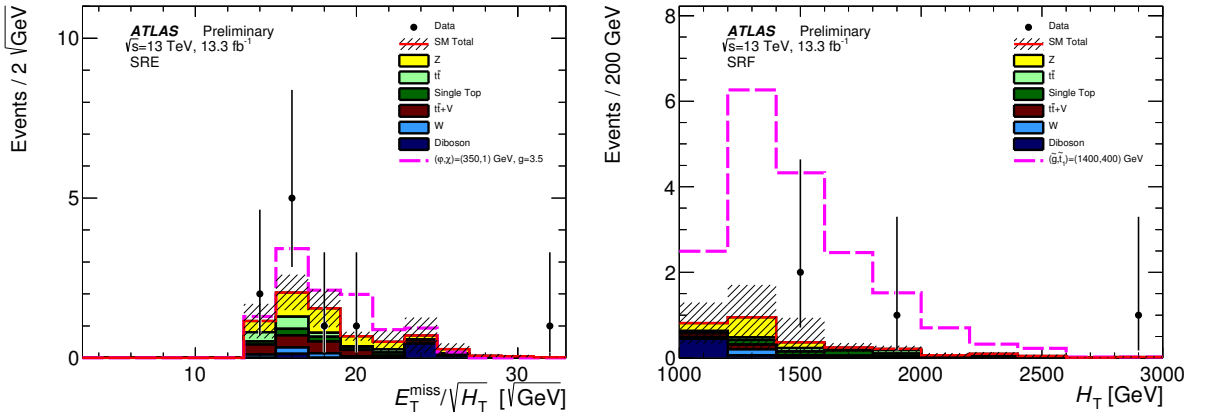


Figure 9: Distributions of $E_T^{\text{miss}} / \sqrt{H_T}$ for SRE and H_T for SRF. The stacked histograms show the SM expectation and the hatched uncertainty band around the SM expectation shows the MC statistical and detector-related systematic uncertainties.

Table 12: Left to right: 95% CL upper limits on the visible cross section ($\langle\epsilon\sigma\rangle_{\text{obs}}^{95}$) and on the number of signal events (S_{obs}^{95}). The third column (S_{exp}^{95}) shows the 95% CL upper limit on the number of signal events, given the expected number (and $\pm 1\sigma$ excursions on the expectation) of background events. The two columns before last indicate the discovery p -value ($p(s = 0)$) and the the significance for the p -value (σ). The p -value is set to 0.50 when the observed event yield is less than the expected event yield.

Signal channel	$\langle\epsilon\sigma\rangle_{\text{obs}}^{95} [\text{fb}]$	S_{obs}^{95}	S_{exp}^{95}	$p(s = 0)$	σ
SRA-TT	0.72	9.5	$6.9_{-2.1}^{+3.3}$	0.18	0.92
SRA-TW	0.46	6.1	$6.6_{-2.0}^{+3.3}$	0.50	0.00
SRA-T0	1.05	14.0	$10.1_{-2.9}^{+4.4}$	0.16	0.99
SRB-TT	1.17	15.5	$10.0_{-2.9}^{+4.3}$	0.08	1.41
SRB-TW	0.97	12.9	$12.1_{-3.5}^{+4.8}$	0.41	0.23
SRB-T0	3.91	52.1	$38.2_{-10.0}^{+12.9}$	0.10	1.28
SRC-low	2.19	29.1	$21.9_{-5.7}^{+7.4}$	0.13	1.13
SRC-med	1.10	14.6	$11.3_{-3.2}^{+4.5}$	0.19	0.88
SRC-high	0.66	8.8	$9.6_{-2.6}^{+3.8}$	0.50	0.00
SRD1	0.45	6.0	$6.1_{-2.0}^{+3.1}$	0.50	0.00
SRD2	0.47	6.2	$7.6_{-2.1}^{+3.1}$	0.50	0.00
SRD3	0.69	9.2	$9.0_{-2.7}^{+3.7}$	0.49	0.03
SRD4	0.67	8.9	$9.2_{-2.7}^{+3.8}$	0.50	0.00
SRD5	0.69	9.2	$9.6_{-2.8}^{+4.1}$	0.50	0.00
SRD6	0.50	6.6	$8.1_{-2.2}^{+3.6}$	0.50	0.00
SRD7	0.50	6.6	$6.8_{-1.9}^{+3.2}$	0.49	0.03
SRD8	0.28	3.7	$4.7_{-1.2}^{+2.6}$	0.50	0.00
SRE	0.72	9.5	$7.9_{-2.3}^{+3.6}$	0.29	0.55
SRF	0.42	5.6	$5.4_{-1.6}^{+2.6}$	0.47	0.08

$m_\varphi = 350$ GeV, $m_\chi = 1$ GeV, and $m_{\tilde{g}} = 1400$ GeV, $m_{\tilde{t}} = 400$ GeV, $m_{\tilde{\chi}^0} = 395$ GeV. SRB and SRC-low have $A \cdot \epsilon$ of 1.2% and 1.3% for $m_{\tilde{t}} = 600$ GeV, $m_{\tilde{\chi}^0} = 300$ GeV and $m_{\tilde{t}} = 700$ GeV, $m_{\tilde{\chi}_1^\pm} = 100$, $m_{\tilde{\chi}^0} = 50$ GeV, respectively. Finally, SRD1-4 and SRD5-8 (combining the R_{ISR} windows) has an $A \cdot \epsilon$ of 0.12% and 0.22% for $m_{\tilde{t}} = 350$ GeV, $m_{\tilde{\chi}^0} = 177$ GeV and $m_{\tilde{t}} = 450$ GeV, $m_{\tilde{\chi}^0} = 277$ GeV.

The profile likelihood ratio test statistic is used to set limits on direct pair production of top squarks. A fixed signal component is used, and any signal contamination in the CRs is taken into account. Again, limits are derived using the CL_s prescription and calculated from asymptotic formulae. Orthogonal signal subregions, such as SRA-TT, SRA-TW, and SRA-T0, are statistically combined by multiplying their likelihood functions. A similar procedure is performed for the signal subregions in SRB. For the overlapping signal subregions defined for SRC and SRD, the signal subregion with the smallest expected 95% CL_s value is chosen for each signal model. Once the signal subregions are combined or chosen, the signal region with the smallest expected 95% CL_s is chosen from SRA, SRB, and SRD for each signal model in the \tilde{t} - $\tilde{\chi}_1^0$ signal grid. The nominal event yield in each SR is set to the mean background expectation to determine the expected limits; contours that correspond to $\pm 1\sigma$ uncertainties in the background estimates (σ_{exp}) are also evaluated. The observed event yields determine the observed limits for each SR; these are evaluated for the nominal signal cross sections as well as for $\pm 1\sigma$ theory uncertainties on those cross sections $\sigma_{\text{theory}}^{\text{SUSY}}$.

Figure 10 (a) shows the observed (solid red line) and expected (dashed blue line) exclusion limits at 95% CL in the \tilde{t} - $\tilde{\chi}_1^0$ mass plane for $\int \mathcal{L} dt = 13.3 \text{ fb}^{-1}$ for SRA, SRB, and SRD. The data excludes top squark masses in the range 310–820 GeV for $\tilde{\chi}_1^0$ masses below 160 GeV extending Run 1 limits by 100 GeV. Additional constraints are set in the case when $m_{\tilde{t}} \sim m_t + m_{\tilde{\chi}^0}$, for which top squark masses between 23–380 GeV are excluded.

For signal models in the b - $\tilde{\chi}_1^\pm$ grid, the signal region with the smallest expected 95% CL_s is chosen from SRB and SRC to yield the combined limit shown in Fig. 11. SRB is most sensitive in near the kinematic boundary of $m_{\tilde{t}} = m_b + m_{\tilde{\chi}_1^\pm}$ while SRC is the most sensitive along low $m_{\tilde{\chi}^0}$. Due to the mild excess in the number of observed events in SRB, the observed 95% CL limit is restricted to $m_{\tilde{\chi}_1^\pm}$ values below 150 GeV while the expected limit extends to higher values.

The results for SRE are interpreted in terms of simplified models of top quarks produced in association with DM particles as a function of the DM and mediator masses, and varying coupling strengths (nominally $g = 3.5$). The exclusion limits on the m_χ vs. m_φ and on the m_χ vs. m_a plane are shown in Fig. 12. In addition to showing limits assuming $g = 3.5$, Fig. 12 also contains upper limits on the coupling, g , indicated by the numbers on the figure, as a function of m_χ and m_a, m_φ . For both the scalar (pseudoscalar) interpretation the most stringent limits on the coupling are at low m_χ and low m_φ (m_a).

The SRF results are interpreted for indirect top squark production through gluino decays in terms of the $\tilde{\chi}_1^0$ vs. \tilde{g} mass plane with $\Delta m(\tilde{t}, \tilde{\chi}_1^0) = 5$ GeV. All grid points up to $m_{\tilde{g}} = 1600$ GeV with $m_{\tilde{\chi}^0} < 560$ GeV are excluded and upper limits on the \tilde{g} pair production cross section are set and shown in Fig. 13.

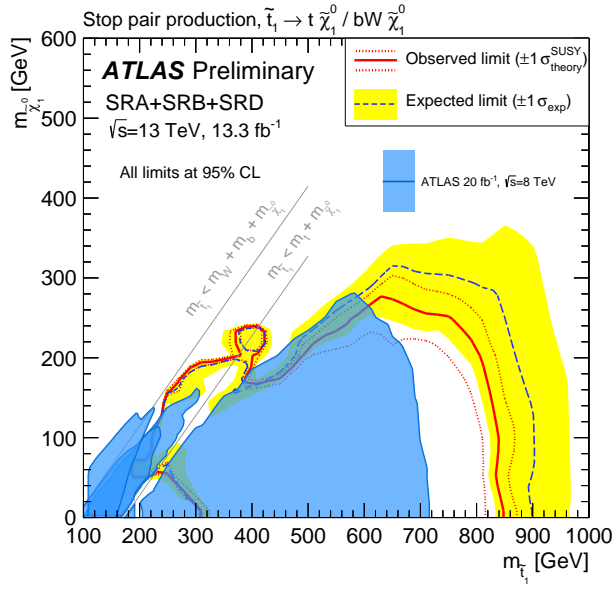


Figure 10: Expected (blue dashed line) and observed (red solid line) exclusion limits at 95% CL as a function of \tilde{t} and $\tilde{\chi}_1^0$ masses in the scenario where both top squarks decay via $\tilde{t} \rightarrow t\tilde{\chi}_1^0$ and the top quark decays hadronically. Uncertainty bands corresponding to the $\pm 1\sigma$ variation on the expected limit (yellow band) and the sensitivity of the observed limit to $\pm 1\sigma$ variations of the signal theoretical uncertainties (red dotted lines) are also indicated. Observed limits from the Run 1 search [19, 72, 73] are overlaid for comparison.

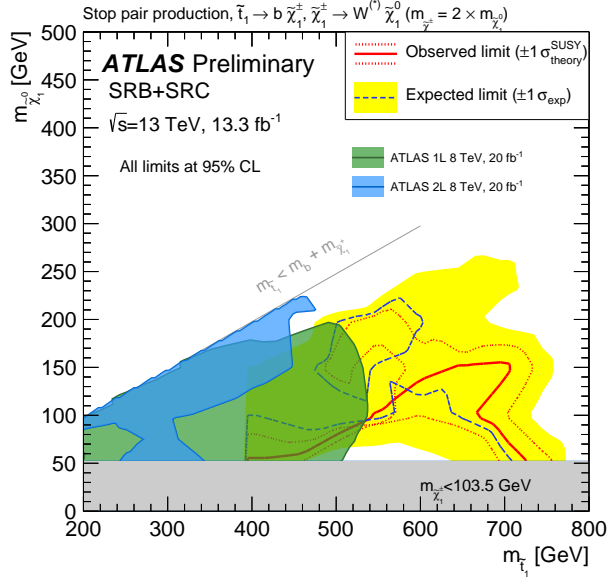


Figure 11: Expected (blue dashed line) and observed (red solid line) exclusion limits at 95% CL as a function of \tilde{t} and $\tilde{\chi}_1^0$ masses in the scenario where both top squarks decay via $\tilde{t} \rightarrow b\tilde{\chi}_1^{\pm}$, $\tilde{\chi}_1^{\pm} \rightarrow W^{(*)}\tilde{\chi}_1^0$ and the $W^{(*)}$ decays hadronically. Uncertainty bands corresponding to the $\pm 1\sigma$ variation on the expected limit (yellow band) and the sensitivity of the observed limit to $\pm 1\sigma$ variations of the signal theoretical uncertainties (red dotted lines) are also indicated. Observed limits from the Run 1 search [73, 74] are overlaid for comparison.

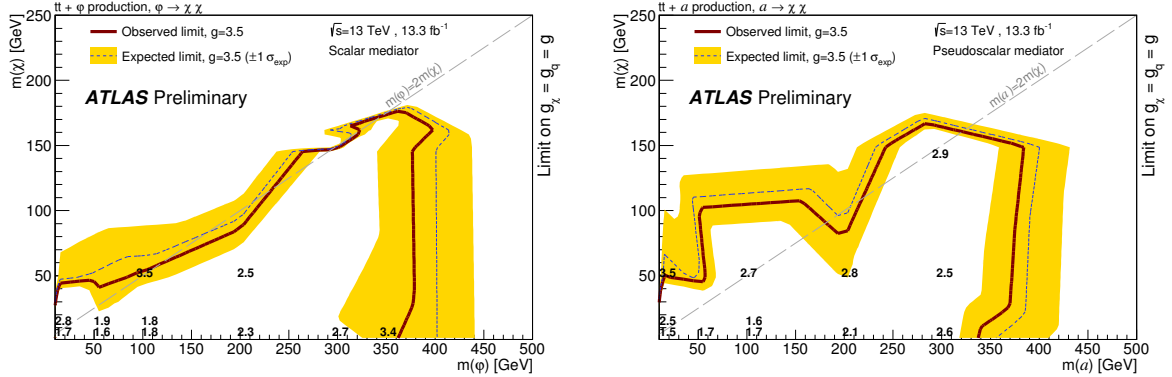


Figure 12: Expected (blue dashed line) and observed (red solid line) $g = 3.5$ exclusion limits at 95% CL as a function of φ and χ masses (left) and a and χ masses (right) in the DM+ $t\bar{t}$ scenario. Uncertainty bands corresponding to the $\pm 1\sigma$ variation on the expected limit (yellow band) and the sensitivity of the observed limit to $\pm 1\sigma$ variations of the signal theoretical uncertainties (red dotted lines) are also indicated. The numbers on the plots indicate the limits on the coupling. Couplings above the perturbativity limit ($g = 3.5$) are not considered.

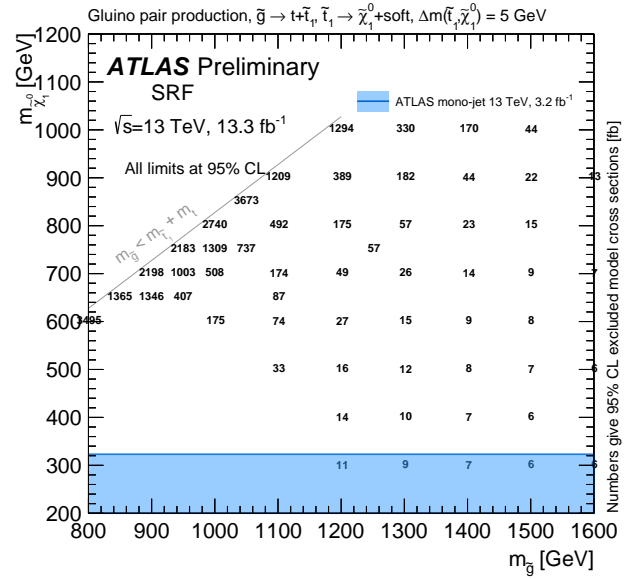


Figure 13: Cross section limits at 95% CL exclusion as a function of \tilde{g} and $\tilde{\chi}_1^0$ masses in the scenario where both gluinos decay via $\tilde{g} \rightarrow t\tilde{t}\tilde{\chi}_1^0 \rightarrow t\tilde{\chi}_1^0 + \text{soft}$ and $\Delta m(\tilde{t}, \tilde{\chi}_1^0) = 5$ GeV.

10. Conclusions

The results from the search for top squark production based on $\int \mathcal{L} dt = (13.3 \pm 0.4) \text{ fb}^{-1}$ data of $\sqrt{s} = 13 \text{ TeV}$ pp collisions recorded by the ATLAS experiment at the LHC in 2015 and 2016 are presented. Top squarks are searched for in final states with high- p_T jets and large missing transverse momentum. In this document, the top squark is assumed to decay via $\tilde{t} \rightarrow t \tilde{\chi}_1^0$ with large or small $\Delta m(\tilde{t}, \tilde{\chi}_1^0)$ and via $\tilde{t} \rightarrow b \tilde{\chi}_1^\pm$. Gluino-mediated \tilde{t} production is studied in which gluinos decay via $\tilde{g} \rightarrow t\tilde{t}$, with a small $\Delta m(\tilde{t}, \tilde{\chi}_1^0)$. Finally, signal models of the associated production of top pairs with a pair of dark matter particles produced through a scalar (pseudoscalar) mediator φ (a) are also taken into consideration.

No significant excess above the expected SM background prediction is observed. Exclusion limits at 95% confidence level on the combination of top squark and LSP mass are derived. Additionally model independent limits and p-values for each signal region are reported. The limits in various interpretations significantly extend previous results.

References

- [1] S. Weinberg, *Implications of Dynamical Symmetry Breaking*, Phys. Rev. **D13** (1976) 974.
- [2] E. Gildener, *Gauge Symmetry Hierarchies*, Phys. Rev. **D14** (1976) 1667.
- [3] S. Weinberg, *Implications of Dynamical Symmetry Breaking: An Addendum*, Phys. Rev. **D19** (1979) 1277.
- [4] L. Susskind, *Dynamics of Spontaneous Symmetry Breaking in the Weinberg-Salam Theory*, Phys. Rev. **D20** (1979) 2619.
- [5] S. Dimopoulos, S. Raby and F. Wilczek, *Supersymmetry and the scale of unification*, Phys. Rev. D **24** (6 1981) 1681,
URL: <http://link.aps.org/doi/10.1103/PhysRevD.24.1681>.
- [6] L. Ibáñez and G. Ross, *Low-energy predictions in supersymmetric grand unified theories*, Physics Letters B **105** (1981) 439, ISSN: 0370-2693,
URL: <http://www.sciencedirect.com/science/article/pii/0370269381912004>.
- [7] S. Dimopoulos and H. Georgi, *Softly broken supersymmetry and SU(5)*, Nuclear Physics B **193** (1981) 150, ISSN: 0550-3213,
URL: <http://www.sciencedirect.com/science/article/pii/0550321381905228>.
- [8] P. Fayet, *Supersymmetry and weak, electromagnetic and strong interactions*, Physics Letters B **64** (1976) 159, ISSN: 0370-2693,
URL: <http://www.sciencedirect.com/science/article/pii/0370269376903191>.
- [9] P. Fayet,
Spontaneously broken supersymmetric theories of weak, electromagnetic and strong interactions, Physics Letters B **69** (1977) 489, ISSN: 0370-2693,
URL: <http://www.sciencedirect.com/science/article/pii/0370269377908528>.
- [10] G. R. Farrar and P. Fayet, *Phenomenology of the production, decay, and detection of new hadronic states associated with supersymmetry*, Physics Letters B **76** (1978) 575, ISSN: 0370-2693,
URL: <http://www.sciencedirect.com/science/article/pii/0370269378908584>.

- [11] W. Beenakker et al., *Stop production at hadron colliders*, *Nucl. Phys. B* **515** (1998) 3.
- [12] W. Beenakker et al., *Supersymmetric top and bottom squark production at hadron colliders*, *JHEP* **08** (2010) 098, arXiv: [1006.4771 \[hep-ph\]](https://arxiv.org/abs/1006.4771).
- [13] W. Beenakker et al., *Squark and gluino hadroproduction*, *Int. J. Mod. Phys. A* **26** (2011) 2637.
- [14] H. Goldberg, *Constraint on the Photino Mass from Cosmology*, *Phys. Rev. Lett.* **50** (19 1983) 1419, URL: <http://link.aps.org/doi/10.1103/PhysRevLett.50.1419>.
- [15] J. Ellis et al., *Supersymmetric relics from the big bang*, *Nuclear Physics B* **238** (1984) 453 , ISSN: 0550-3213, URL: <http://www.sciencedirect.com/science/article/pii/0550321384904619>.
- [16] T. Lin, E. W. Kolb and L.-T. Wang, *Probing dark matter couplings to top and bottom quarks at the LHC*, *Phys. Rev. D* **88** (2013) 063510, arXiv: [1303.6638 \[hep-ph\]](https://arxiv.org/abs/1303.6638).
- [17] D. Abercrombie et al., *Dark Matter Benchmark Models for Early LHC Run-2 Searches: Report of the ATLAS/CMS Dark Matter Forum*, (2015), ed. by A. Boveia et al., arXiv: [1507.00966 \[hep-ex\]](https://arxiv.org/abs/1507.00966).
- [18] ATLAS Collaboration, *Search for a supersymmetric partner to the top quark in final states with jets and missing transverse momentum at $\sqrt{s} = 7$ TeV with the ATLAS detector*, *Phys. Rev. Lett.* **109** (2012) 211802, arXiv: [1208.1447 \[hep-ex\]](https://arxiv.org/abs/1208.1447).
- [19] ATLAS Collaboration, *Search for direct pair production of the top squark in all-hadronic final states in proton-proton collisions at $\sqrt{s} = 8$ TeV with the ATLAS detector*, *JHEP* **09** (2014) 015, arXiv: [1406.1122 \[hep-ex\]](https://arxiv.org/abs/1406.1122).
- [20] CMS Collaboration, *Inclusive search for supersymmetry using the razor variables in pp collisions at $\sqrt{s} = 7$ TeV*, *Phys. Rev. Lett.* **111** (2013) 081802, arXiv: [1212.6961 \[hep-ex\]](https://arxiv.org/abs/1212.6961).
- [21] CMS Collaboration, *Search for supersymmetry in final states with missing transverse energy and 0, 1, 2, or at least 3 b-quark jets in 7 TeV pp collisions using the variable alphaT*, *JHEP* **01** (2013) 077, arXiv: [1210.8115 \[hep-ex\]](https://arxiv.org/abs/1210.8115).
- [22] CMS Collaboration, *Search for supersymmetry in hadronic final states with missing transverse energy using the variables α_T and b-quark multiplicity in pp collisions at $\sqrt{s} = 8$ TeV*, *Eur. Phys. J. C* **73** (2013) 2568, arXiv: [1303.2985 \[hep-ex\]](https://arxiv.org/abs/1303.2985).
- [23] CMS Collaboration, *Searches for third-generation squark production in fully hadronic final states in proton-proton collisions at $\sqrt{s} = 8$ TeV*, *JHEP* **06** (2015) 116, arXiv: [1503.08037 \[hep-ex\]](https://arxiv.org/abs/1503.08037).
- [24] CMS Collaboration, *Search for direct pair production of supersymmetric top quarks decaying to all-hadronic final states in pp collisions at $\sqrt{s} = 8$ TeV*, (2016), arXiv: [1603.00765 \[hep-ex\]](https://arxiv.org/abs/1603.00765).
- [25] CMS Collaboration, *Search for new physics with the MT2 variable in all-jets final states produced in pp collisions at $\sqrt{s} = 13$ TeV*, (2016), arXiv: [1603.04053 \[hep-ex\]](https://arxiv.org/abs/1603.04053).
- [26] ATLAS Collaboration, *The ATLAS Experiment at the CERN Large Hadron Collider*, *JINST* **3** (2008) S08003.
- [27] ATLAS Collaboration, *ATLAS Insertable B-Layer Technical Design Report*, (2010), URL: <https://cds.cern.ch/record/1291633>.

[28] ATLAS Collaboration, *Improved luminosity determination in pp collisions at $\sqrt{s} = 7$ TeV using the ATLAS detector at the LHC*, *Eur. Phys. J.* **C73** (2013) 2518, arXiv: [1302.4393 \[hep-ex\]](https://arxiv.org/abs/1302.4393).

[29] ATLAS Collaboration, *Luminosity determination in pp collisions at $\sqrt{s} = 8$ TeV using the ATLAS detector at the LHC*, to be submitted to *Eur. Phys. J.* () .

[30] U. Haisch and E. Re, *Simplified dark matter top-quark interactions at the LHC*, *JHEP* **06** (2015) 078, arXiv: [1503.00691 \[hep-ph\]](https://arxiv.org/abs/1503.00691).

[31] M. R. Buckley, D. Feld and D. Goncalves, *Scalar Simplified Models for Dark Matter*, *Phys. Rev.* **D91** (2015) 015017, arXiv: [1410.6497 \[hep-ph\]](https://arxiv.org/abs/1410.6497).

[32] J. Alwall et al., *The automated computation of tree-level and next-to-leading order differential cross sections, and their matching to parton shower simulations*, *JHEP* **07** (2014) 079, arXiv: [1405.0301 \[hep-ph\]](https://arxiv.org/abs/1405.0301).

[33] T. Sjostrand, S. Mrenna and P. Z. Skands, *A Brief Introduction to PYTHIA 8.1*, *Comput. Phys. Commun.* **178** (2008) 852, arXiv: [0710.3820 \[hep-ph\]](https://arxiv.org/abs/0710.3820).

[34] D. J. Lange, *The EvtGen particle decay simulation package*, *Nuclear Instruments and Methods in Physics Research Section A: Accelerators, Spectrometers, Detectors and Associated Equipment* **462** (2001) 152, BEAUTY2000, Proceedings of the 7th Int. Conf. on B-Physics at Hadron Machines, ISSN: 0168-9002, URL: <http://www.sciencedirect.com/science/article/pii/S0168900201000894>.

[35] R. D. Ball et al., *Parton distributions with LHC data*, *Nucl. Phys. B* **867** (2013) 244, arXiv: [1207.1303 \[hep-ph\]](https://arxiv.org/abs/1207.1303).

[36] ATLAS Collaboration, *ATLAS Run 1 Pythia8 tunes*, (2014), URL: <https://cds.cern.ch/record/1966419>.

[37] L. Lönnblad and S. Prestel, *Merging Multi-leg NLO Matrix Elements with Parton Showers*, *JHEP* **03** (2013) 166, arXiv: [1211.7278 \[hep-ph\]](https://arxiv.org/abs/1211.7278).

[38] M. Kramer et al., *Supersymmetry production cross sections in pp collisions at $\sqrt{s} = 7$ TeV*, (2012), arXiv: [1206.2892 \[hep-ph\]](https://arxiv.org/abs/1206.2892).

[39] T. Gleisberg et al., *Event generation with SHERPA 1.1*, *JHEP* **02** (2009) 007, arXiv: [0811.4622 \[hep-ph\]](https://arxiv.org/abs/0811.4622).

[40] S. Alioli et al., *A general framework for implementing NLO calculations in shower Monte Carlo programs: the POWHEG BOX*, *JHEP* **06** (2010) 043, arXiv: [1002.2581 \[hep-ph\]](https://arxiv.org/abs/1002.2581).

[41] T. Sjöstrand, S. Mrenna and P. Skands, *PYTHIA 6.4 Physics and Manual*, *JHEP* **05** (2006) 026, arXiv: [hep-ph/0603175](https://arxiv.org/abs/hep-ph/0603175).

[42] H.-L. Lai et al., *New parton distributions for collider physics*, *Phys. Rev. D* **82** (2010) 074024, arXiv: [1007.2241 \[hep-ph\]](https://arxiv.org/abs/1007.2241).

[43] P. Z. Skands, *Tuning Monte Carlo Generators: The Perugia Tunes*, *Phys. Rev. D* **82** (2010) 074018, arXiv: [1005.3457 \[hep-ph\]](https://arxiv.org/abs/1005.3457).

[44] G. G. Hesketh et al., *Monte Carlo Generators for the Production of a W or Z/γ^* Boson in Association with Jets at ATLAS in Run 2*, (2016), URL: <https://cds.cern.ch/record/2120133>.

[45] C. Gutschow et al., *Multi-Boson Simulation for 13 TeV ATLAS Analyses*, (2016), URL: <https://cds.cern.ch/record/2119986>.

[46] B. P. Nachman and A. Knue, *Simulation of top quark production for the ATLAS experiment at $\sqrt{s} = 13$ TeV*, (2016), URL: <https://cds.cern.ch/record/2120417>.

[47] J. Mcfayden et al., *Modelling of the $t\bar{t}H$ and $t\bar{t}V$ ($V = W, Z$) processes for $\sqrt{s} = 13$ TeV ATLAS analyses*, (2016), URL: <https://cds.cern.ch/record/2120826>.

[48] M. Moreno Llacer and L. Serkin, *Validation of Monte Carlo event generators in the ATLAS Collaboration for LHC Run 2*, (2016), URL: <https://cds.cern.ch/record/2119984>.

[49] ATLAS Collaboration, *The ATLAS Simulation Infrastructure*, *Eur. Phys. J.* **C70** (2010) 823, arXiv: [1005.4568 \[physics.ins-det\]](https://arxiv.org/abs/1005.4568).

[50] S. Agostinelli et al., *GEANT4: A Simulation toolkit*, *Nucl. Instrum. Meth.* **A506** (2003) 250.

[51] ATLAS Collaboration, *The simulation principle and performance of the ATLAS fast calorimeter simulation FastCaloSim*, (2010), URL: <https://cds.cern.ch/record/1300517>.

[52] ATLAS Collaboration, *Vertex Reconstruction Performance of the ATLAS Detector at $\sqrt{s} = 13$ TeV*, (2015), URL: <https://cds.cern.ch/record/2037717>.

[53] W Lampl et al., *Calorimeter Clustering Algorithms: Description and Performance*, (2008), URL: <https://cds.cern.ch/record/1099735>.

[54] M. Cacciari, G. P. Salam and G. Soyez, *The Anti- $k(t)$ jet clustering algorithm*, *JHEP* **04** (2008) 063, arXiv: [0802.1189 \[hep-ph\]](https://arxiv.org/abs/0802.1189).

[55] M. Cacciari and G. P. Salam, *Pileup subtraction using jet areas*, *Phys. Lett.* **B659** (2008) 119, arXiv: [0707.1378 \[hep-ph\]](https://arxiv.org/abs/0707.1378).

[56] ATLAS Collaboration, *Jet Calibration and Systematic Uncertainties for Jets Reconstructed in the ATLAS Detector at $\sqrt{s} = 13$ TeV*, (2015), URL: <https://cds.cern.ch/record/2037613>.

[57] ATLAS Collaboration, *Selection of jets produced in 13TeV proton-proton collisions with the ATLAS detector*, (2015), URL: <https://cds.cern.ch/record/2037702>.

[58] ATLAS Collaboration, *Tagging and suppression of pileup jets with the ATLAS detector*, (2014), URL: <https://cds.cern.ch/record/1700870>.

[59] ATLAS Collaboration, *Commissioning of the ATLAS b-tagging algorithms using $t\bar{t}$ events in early Run-2 data*, (2015), URL: <https://cds.cern.ch/record/2047871>.

[60] ATLAS Collaboration, *Optimisation of the ATLAS b-tagging performance for the 2016 LHC Run*, (2016), URL: <https://cds.cern.ch/record/2160731>.

[61] ATLAS Collaboration, *b-tagging in dense environments*, (2014), URL: <https://cds.cern.ch/record/1750682>.

[62] ATLAS Collaboration, *Performance of Missing Transverse Momentum Reconstruction in ATLAS studied in Proton-Proton Collisions recorded in 2012 at 8 TeV*, (2013), URL: <https://cds.cern.ch/record/1570993>.

[63] ATLAS Collaboration, *Muon reconstruction performance of the ATLAS detector in proton–proton collision data at $\sqrt{s} = 13$ TeV*, (2016), arXiv: [1603.05598 \[hep-ex\]](https://arxiv.org/abs/1603.05598), *PERF-2015-10*.

[64] H. An and L.-T. Wang, *Opening up the compressed region of top squark searches at 13 TeV LHC*, *Phys. Rev. Lett.* **115** (2015) 181602, arXiv: [1506.00653 \[hep-ph\]](https://arxiv.org/abs/1506.00653).

[65] S. Macaluso et al., *Revealing Compressed Stops Using High-Momentum Recoils*, *JHEP* **03** (2016) 151, arXiv: [1506.07885 \[hep-ph\]](https://arxiv.org/abs/1506.07885).

[66] P. Jackson, C. Rogan and M. Santoni, *Sparticles in Motion - getting to the line in compressed scenarios with the Recursive Jigsaw Reconstruction*, (2016), arXiv: [1607.08307 \[hep-ph\]](https://arxiv.org/abs/1607.08307).

[67] ATLAS Collaboration, *Search for squarks and gluinos with the ATLAS detector in final states with jets and missing transverse momentum using 4.7 fb^{-1} of $\sqrt{s} = 7$ TeV proton-proton collision data*, *Phys. Rev. D* **87** (2013) 012008, arXiv: [1208.0949 \[hep-ex\]](https://arxiv.org/abs/1208.0949).

[68] G. Cowan et al., *Asymptotic formulae for likelihood-based tests of new physics*, *Eur. Phys. J. C* **71** (2011) 1554, [Erratum: *Eur. Phys. J.* C73,2501(2013)], arXiv: [1007.1727 \[physics.data-an\]](https://arxiv.org/abs/1007.1727).

[69] M. Baak et al., *HistFitter software framework for statistical data analysis*, *Eur. Phys. J. C* **75** (2015) 153, arXiv: [1410.1280 \[hep-ex\]](https://arxiv.org/abs/1410.1280).

[70] T. Junk, *Confidence level computation for combining searches with small statistics*, *Nucl. Instrum. Meth. A* **434** (1999) 435, arXiv: [hep-ex/9902006 \[hep-ex\]](https://arxiv.org/abs/hep-ex/9902006).

[71] A. L. Read, *Presentation of search results: the CL s technique*, *Journal of Physics G: Nuclear and Particle Physics* **28** (2002) 2693, URL: <http://stacks.iop.org/0954-3899/28/i=10/a=313>.

[72] ATLAS Collaboration, *ATLAS Run 1 searches for direct pair production of third-generation squarks at the Large Hadron Collider*, *Eur. Phys. J. C* **75** (2015) 510, [Erratum: *Eur. Phys. J.* C76,no.3,153(2016)], arXiv: [1506.08616 \[hep-ex\]](https://arxiv.org/abs/1506.08616).

[73] ATLAS Collaboration, *Search for top squark pair production in final states with one isolated lepton, jets, and missing transverse momentum in $\sqrt{s} = 8$ TeV pp collisions with the ATLAS detector*, *JHEP* **11** (2014) 118, arXiv: [1407.0583 \[hep-ex\]](https://arxiv.org/abs/1407.0583).

[74] ATLAS Collaboration, *Search for direct top-squark pair production in final states with two leptons in pp collisions at $\sqrt{s} = 8$ TeV with the ATLAS detector*, *JHEP* **06** (2014) 124, arXiv: [1403.4853 \[hep-ex\]](https://arxiv.org/abs/1403.4853).

A. Appendix

A.1. Validation Regions

To validate the $Z +$ jets background estimates in SRA–C, E, and F, regions VRZ-A through VRZ-F are defined as shown in Table 13. The criteria listed are in addition to the CRZ selection criteria shown in Table 5. The $W +$ jets background estimate is validated by applying the same selection criteria as in CRW, except that at least 2 b -tagged jets are required, $m_{\text{jet},R=1.2}^0 < 70 \text{ GeV}$, $m_{\text{T}}^{b,\text{min}} > 150 \text{ GeV}$, and $\Delta R(b, \ell)_{\text{min}} > 1.8$. This criteria ensures that the flavor composition in the VRW validation region is similar to that in the signal regions. Data/simulation comparisons from VRZ-A and VRW are shown in Fig. 14.

Table 13: Selection criteria for the $Z +$ jets validation regions corresponding to SRA–C, SRE and SRF. The criteria listed are in addition to those applied to CRZ.

Selection	VRZA	VRZB	VRZC	VRZE	VRZF
$E_{\text{T}}^{\text{miss}'}$	$> 200 \text{ GeV}$				
$m_{\text{T}}^{b,\text{min}}$	$> 100 \text{ GeV}$				
$m_{\text{jet},R=1.2}^0$	$> 60 \text{ GeV}$	$> 60 \text{ GeV}$	-	$> 60 \text{ GeV}$	-
$\Delta R(b, b)$	-	> 0.8	> 0.8	> 0.8	-
$m_{\text{T}}^{b,\text{max}}$	-	$> 100 \text{ GeV}$	$> 200 \text{ GeV}$	$> 100 \text{ GeV}$	-
H_{T}	-	-	-	-	$> 300 \text{ GeV}$
$E_{\text{T}}^{\text{miss}} / \sqrt{H_{\text{T}}}$	-	-	-	$> 10 \sqrt{\text{GeV}}$	$> 8 \sqrt{\text{GeV}}$
$m_{\text{jet},R=0.8}^0$	-	-	-	-	$> 30 \text{ GeV}$

The $t\bar{t}$ background estimate is validated by defining several kinematic regions. In addition to the common all-hadronic preselection requirements, VRT-low (VRT-high) is required to have $E_{\text{T}}^{\text{miss}} > 250 \text{ GeV}$ ($E_{\text{T}}^{\text{miss}} > 350 \text{ GeV}$) and is kinematically similar to SRB, SRC, and SRE (SRA and SRF). The events in VRT-low and VRT-high must have at least 2 b -tagged jets and an orthogonal $m_{\text{T}}^{b,\text{min}}$ requirement: $50 < m_{\text{T}}^{b,\text{min}} < 150 \text{ GeV}$. Estimates of the $t\bar{t}$ background contribution in SRD are validated using two regions: VRT-ISR-1b and VRT-ISR-2b, which require at least 1 and at least 2 b -tagged jets, and correspond to SRD5-8 and SRD1-4, respectively. A requirement of $R_{\text{ISR}} > 0.45$ is applied to VRT-ISR-1b. For both regions, the M_{T}^S requirement is relaxed to $M_{\text{T}}^S > 100 \text{ GeV}$, the N_{jet}^S requirement is relaxed to $N_{\text{jet}}^S \geq 4$, and the $p_{\text{T}}^{\text{jet}4,S}$ requirement is removed. An additional requirement on the ratio of the transverse mass of the visible part of the sparticle system ($M_{\text{T}}^{S,\text{Vis}}$) to M_{T}^S is imposed: $M_{\text{T}}^{S,\text{Vis}} / M_{\text{T}}^S < 0.6$ to reduce signal and multijet contamination. Finally, the $p_{\text{T}}^{\text{ISR}}$ requirement is inverted compared to the signal region; both validation regions require $p_{\text{T}}^{\text{ISR}} < 3.0$. Data/simulation comparisons from VRT-low, VRT-high, VRT-ISR-1b, and VRT-ISR-2b are shown in Fig. 15.

The background yield in each validation region is predicted from the combined fit to the control regions. The resulting estimate is consistent with the observed number of events in data; these results are

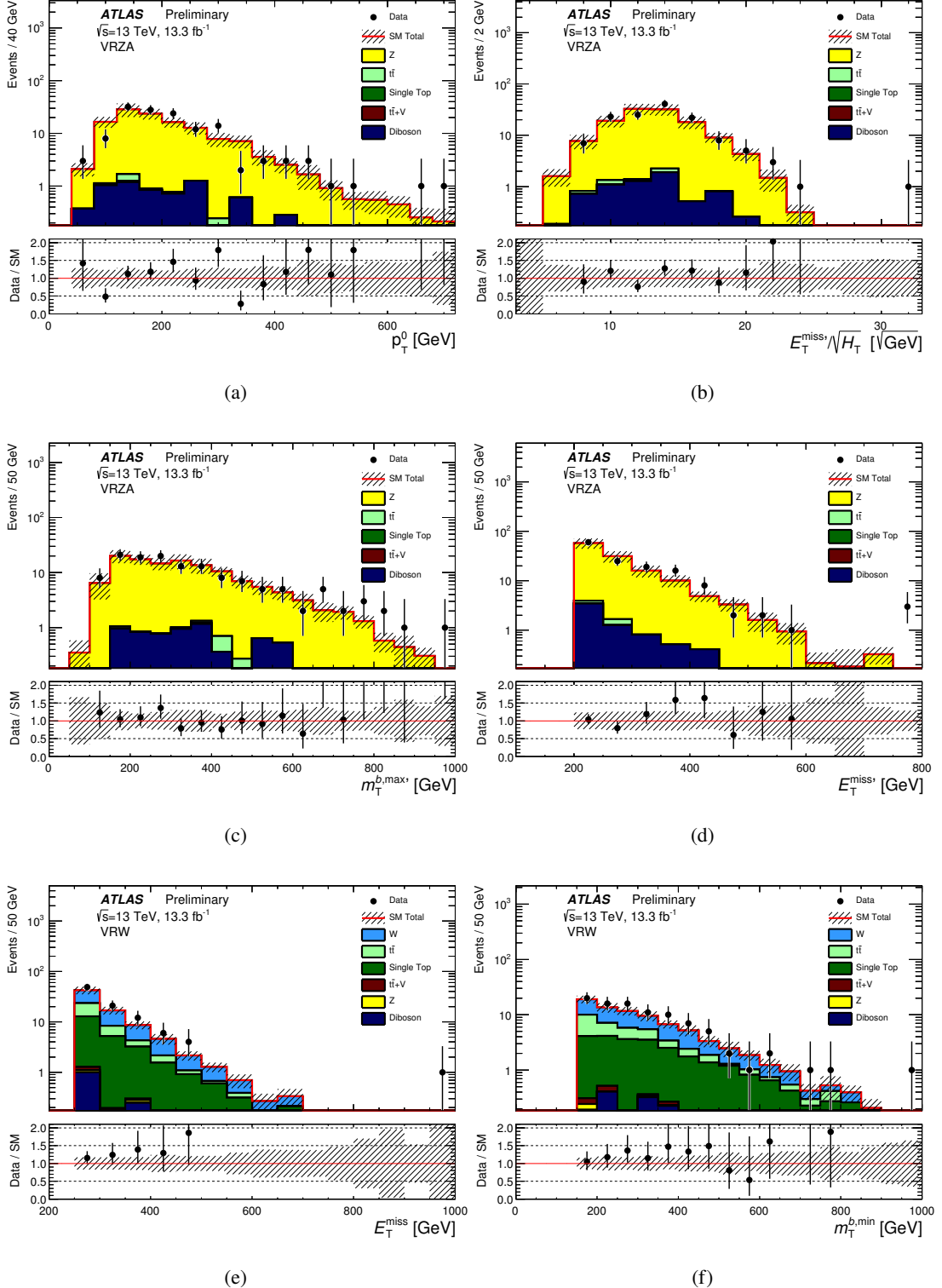


Figure 14: Distributions of (a) p_T of the leading jet, (b) $E_T^{\text{miss}}/\sqrt{H_T}$, (c) $m_T^{b,\text{max}}$ and (d) $E_T^{\text{miss}'}$ in the VRZA, and (e) E_T^{miss} and (f) the fourth-leading jet p_T in VRW. The stacked histograms show the SM expectation, normalized using scale factors derived from the simultaneous fit to all backgrounds. The “Data/SM” plots show the ratio of data events to the total SM expectation. The hatched uncertainty band around the SM expectation and in the ratio plots illustrates the combination of MC statistical and detector-related systematic uncertainties. The rightmost bin includes all overflows.

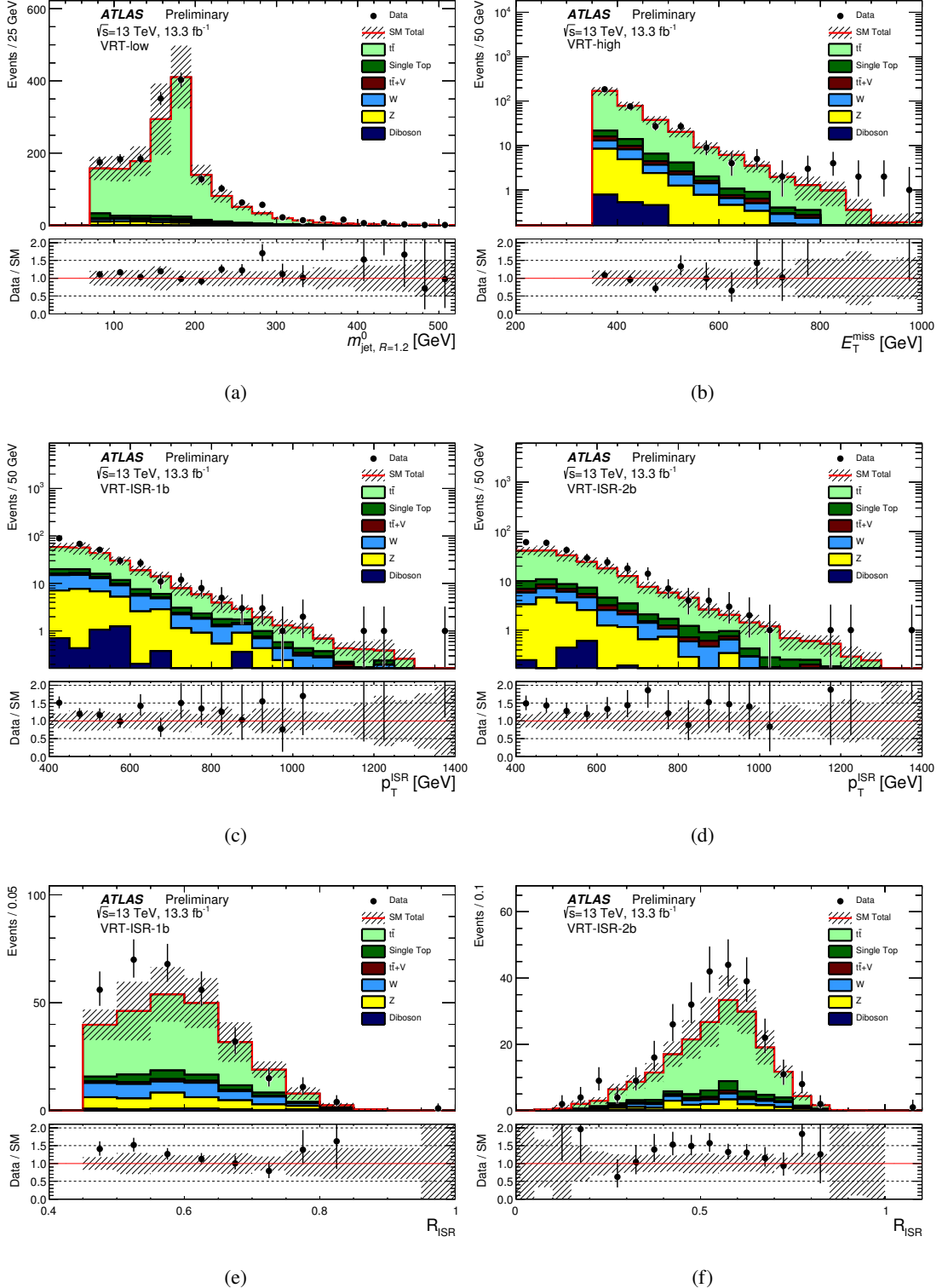


Figure 15: Distributions of (a) $m_{\text{jet}, R=1.2}^0$ in VRT-low, (b) $E_{\text{T}}^{\text{miss}}$ in VRT-high, (c) $p_{\text{T}}^{\text{ISR}}$ in VRT-ISR-1b, (d) $p_{\text{T}}^{\text{ISR}}$ VRT-ISR-2b, (e) R_{ISR} in VRT-ISR-1b, and (f) R_{ISR} in VRT-ISR-2b. The stacked histograms show the SM expectation, normalized using scale factors derived from the simultaneous fit to all backgrounds. The “Data/SM” plots show the ratio of data events to the total SM expectation. The hatched uncertainty band around the SM expectation and in the ratio plots illustrates the combination of MC statistical and detector-related systematic uncertainties. The rightmost bin includes all overflows.

summarized in Tables 14 and 15.

Table 14: Event yields in the $Z + \text{jets}$ validation regions compared to the background estimates obtained from the profile likelihood fit. Statistical and systematic uncertainties in the number of fitted background events are shown.

	VRZA	VRZB	VRZC	VRZE	VRZF
Observed	135	104	164	92	117
Total SM	127 \pm 31	94 \pm 23	156 \pm 36	80 \pm 20	110 \pm 26
$t\bar{t}$	0.80 \pm 0.22	0.80 \pm 0.22	0.75 \pm 0.28	0.54 \pm 0.19	0.61 \pm 0.18
$W + \text{jets}$	--	--	--	--	--
$Z + \text{jets}$	119 \pm 32	89 \pm 24	148 \pm 37	76 \pm 21	103 \pm 26
$t\bar{t} + W/Z$	< 0.01	< 0.01	< 0.01	< 0.01	--
Single top	0.06 \pm 0.04	0.06 \pm 0.04	0.06 \pm 0.05	0.06 \pm 0.04	0.06 \pm 0.04
Dibosons	6.8 \pm 1.5	4.6 \pm 1.0	8.0 \pm 1.5	3.66 \pm 0.78	6.4 \pm 1.2
Multijets	--	--	--	--	--

Table 15: Event yields in the $t\bar{t}$ and W validation regions compared to the background estimates obtained from the profile likelihood fit. Statistical and systematic uncertainties in the number of fitted background events are shown.

	VRT-low	VRT-high	VRW	VRT-ISR-2b	VRT-ISR-1b
Observed	1735	345	92	270	312
Total SM	1564 \pm 350	330 \pm 71	77 \pm 14	199 \pm 42	252 \pm 58
$t\bar{t}$	1379 \pm 330	278 \pm 65	15.8 \pm 4.0	144 \pm 40	158 \pm 45
$W + \text{jets}$	40 \pm 10	11.3 \pm 2.8	36.8 \pm 8.6	14.0 \pm 4.1	34 \pm 11
$Z + \text{jets}$	58 \pm 17	17.2 \pm 4.5	0.16 \pm 0.08	17.4 \pm 4.2	32 \pm 12
$t\bar{t} + W/Z$	22.9 \pm 3.0	6.32 \pm 0.81	0.27 \pm 0.05	6.1 \pm 1.5	5.4 \pm 1.4
Single top	57 \pm 24	14.7 \pm 6.3	23 \pm 10	13.8 \pm 5.3	16.5 \pm 6.8
Dibosons	5.1 \pm 1.1	2.06 \pm 0.54	1.50 \pm 0.26	1.98 \pm 0.56	4.9 \pm 2.6
Multijets	1.0 $^{+ 2.1}_{- 1.0}$	0.17 $^{+ 0.35}_{- 0.17}$	--	1.3 $^{+ 2.7}_{- 1.3}$	0.7 $^{+ 1.4}_{- 0.7}$

A.2. Additional figures

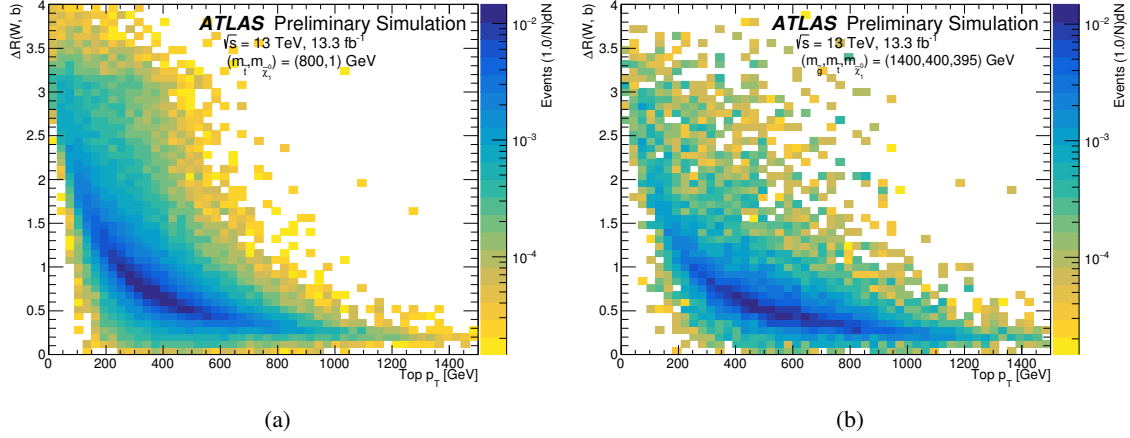


Figure 16: The true ΔR between the W and the b -quark vs. the true top p_T in (a) simulated top squark pair production with $(\tilde{t}, \tilde{\chi}_1^0) = (800, 1) \text{ GeV}$ and (b) simulated top squark production through gluino decays with $(\tilde{g}, \tilde{t}, \tilde{\chi}_1^0) = (1400, 400, 395) \text{ GeV}$. The common preselection criteria are applied with the exception of the b -jet requirement. The histograms are normalized to unity to illustrate the increased boost of the top quarks in the gluino-mediated top squark decays compared to direct top squark production.

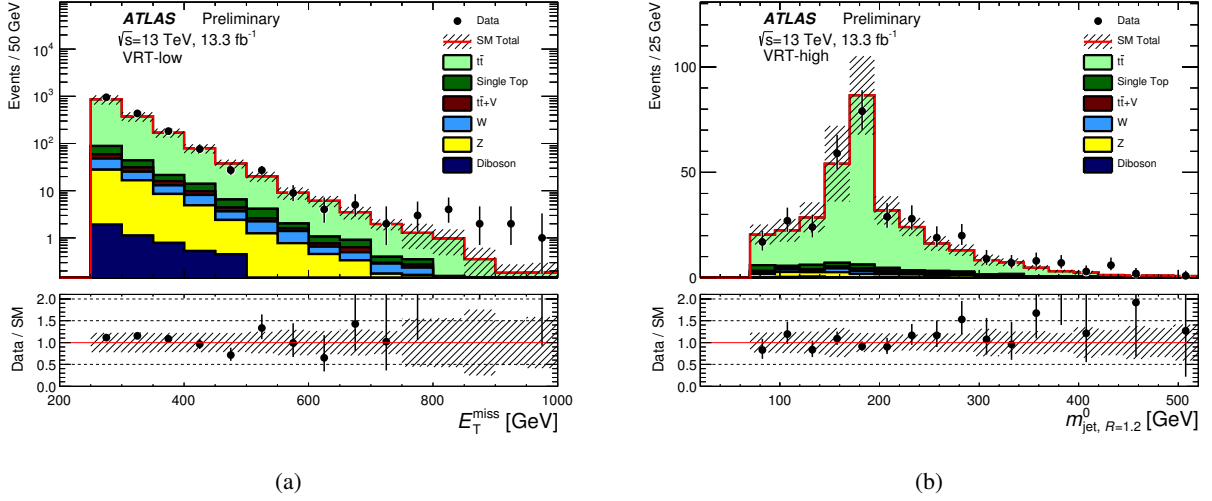


Figure 17: Distributions of (a) E_T^{miss} in VRT-low and (b) $m_{\text{jet}, R=1.2}^0$ in VRT-high. The stacked histograms show the SM expectation, normalized using scale factors derived from the simultaneous fit to all backgrounds. The “Data/SM” plots show the ratio of data events to the total SM expectation. The hatched uncertainty band around the SM expectation and in the ratio plots illustrates the combination of MC statistical and detector-related systematic uncertainties. The rightmost bin includes all overflows.

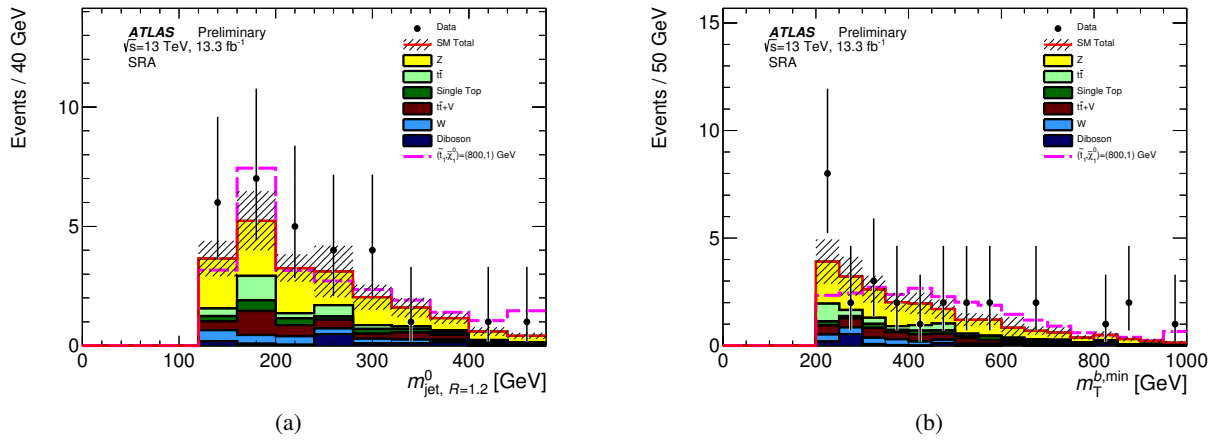


Figure 18: Distributions of (a) $m_{\text{jet}, R=1.2}^0$ and (b) $m_T^{b,\text{min}}$ in SRA. The stacked histograms show the SM expectation and the hatched uncertainty band around the SM expectation shows the MC statistical and detector-related systematic uncertainties.

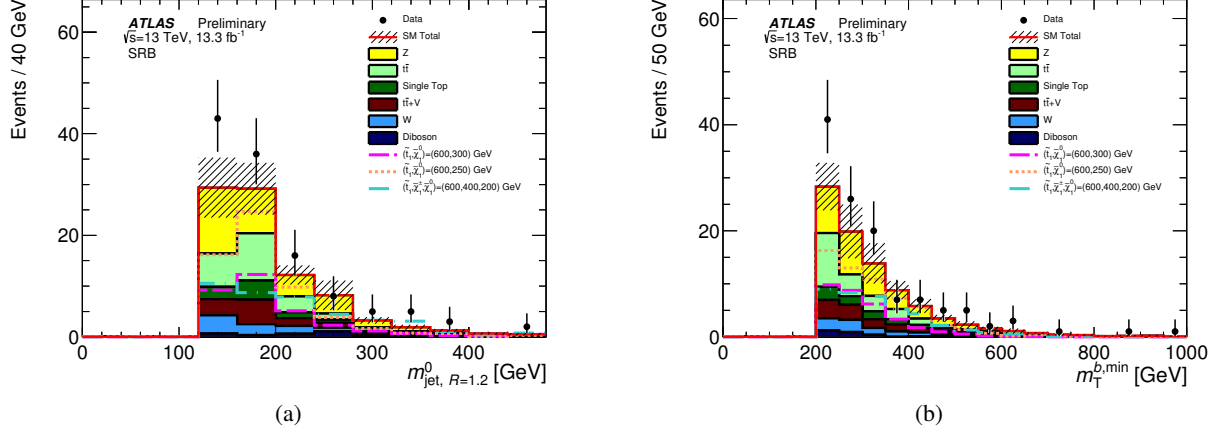


Figure 19: Distributions of (a) $m_{\text{jet}, R=1.2}^0$ and (b) $m_T^{b,\text{min}}$ in SRB. The stacked histograms show the SM expectation and the hatched uncertainty band around the SM expectation shows the MC statistical and detector-related systematic uncertainties.

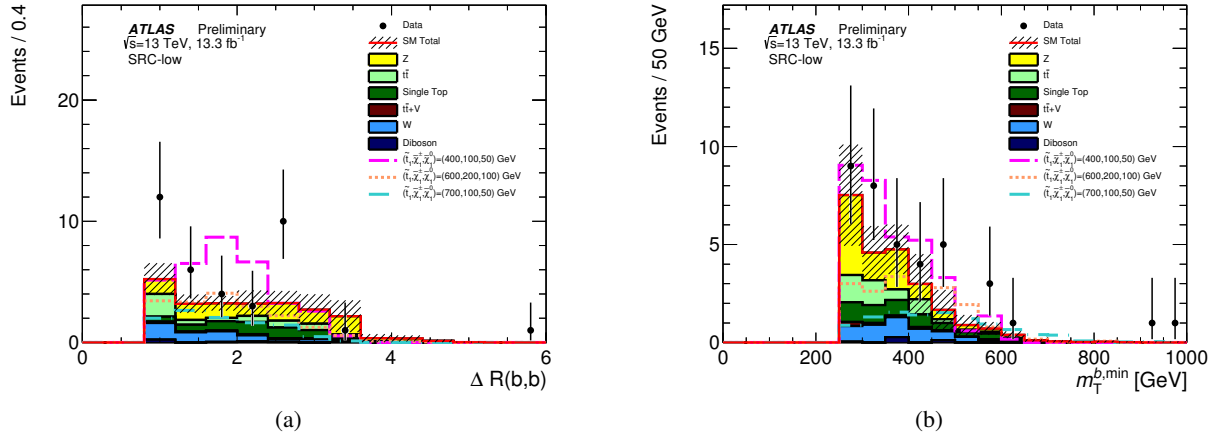


Figure 20: Distributions of (a) $\Delta R(b, b)$ and (b) $m_T^{b,\text{min}}$ in SRC. The stacked histograms show the SM expectation and the hatched uncertainty band around the SM expectation shows the MC statistical and detector-related systematic uncertainties.

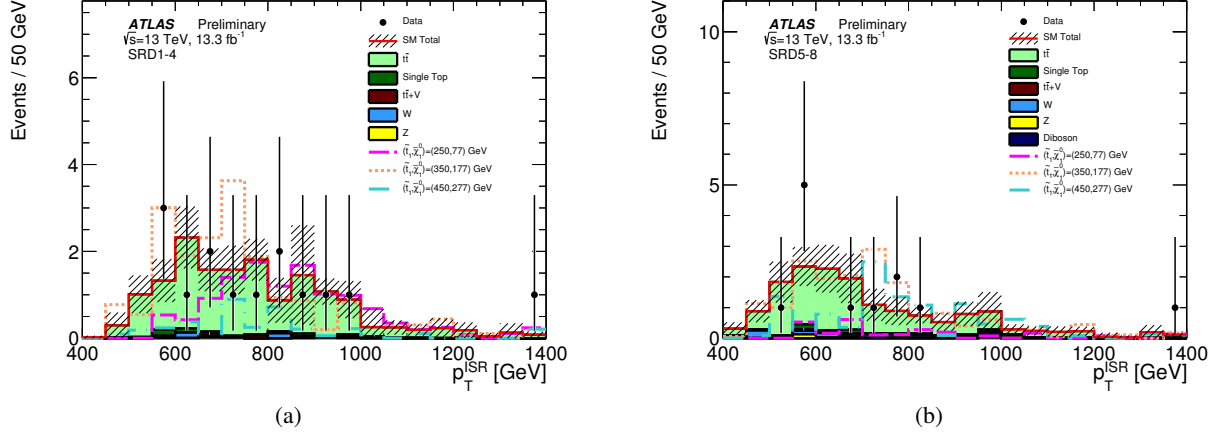


Figure 21: Distributions of p_T^{ISR} in (a) SRD1-4 and (b) SRD5-8. The stacked histograms show the SM expectation and the hatched uncertainty band around the SM expectation shows the MC statistical and detector-related systematic uncertainties.

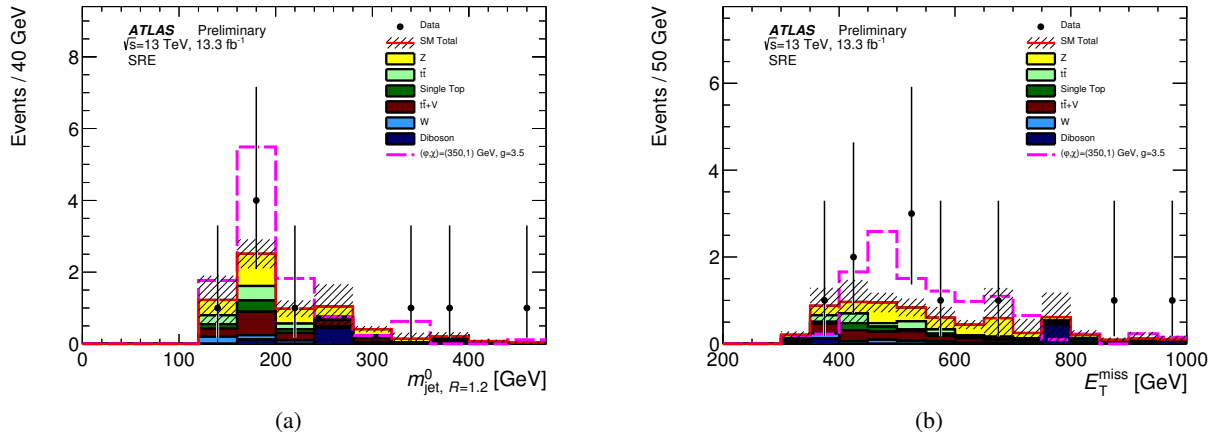


Figure 22: Distributions of (a) $m_{\text{jet}, R=1.2}^0$ and (b) E_T^{miss} in SRE. The stacked histograms show the SM expectation and the hatched uncertainty band around the SM expectation shows the MC statistical and detector-related systematic uncertainties.

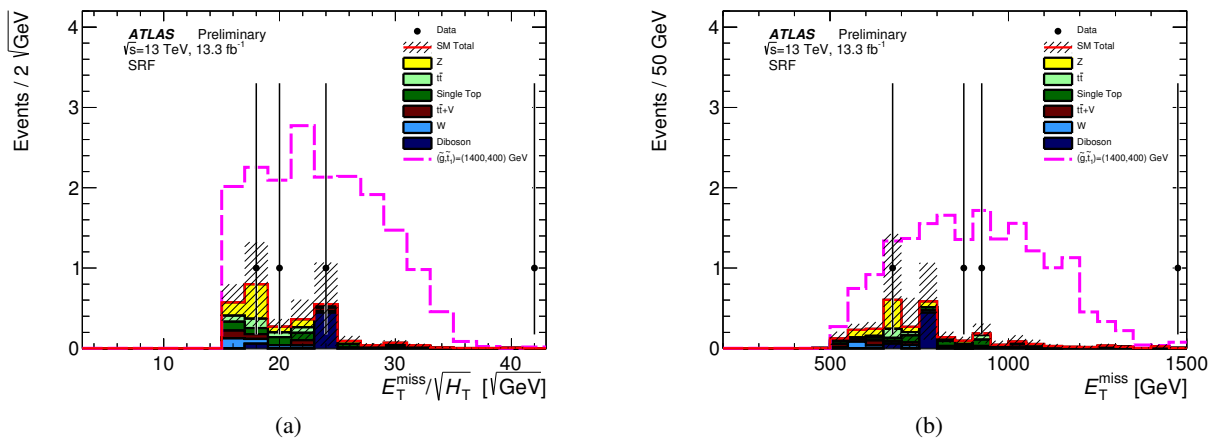


Figure 23: Distributions of (a) $E_T^{\text{miss}} / \sqrt{H_T}$ and (b) E_T^{miss} in SRF. The stacked histograms show the SM expectation and the hatched uncertainty band around the SM expectation shows the MC statistical and detector-related systematic uncertainties.